

**SPECTRAL TIMING STUDIES OF X-RAY BINARIES
OBSERVED WITH ASTROSAT**

**A THESIS SUBMITTED IN PARTIAL FULFILLMENT OF THE
REQUIREMENTS FOR THE DEGREE OF DOCTOR OF
PHILOSOPHY**

VANZARMAWII

MZU REGISTRATION NUMBER : 1807323

Ph.D. REGISTRATION NUMBER : MZU/Ph.D./1263 of 16.08.2018



**DEPARTMENT OF PHYSICS
SCHOOL OF PHYSICAL SCIENCES
APRIL, 2024**

SPECTRAL TIMING STUDIES OF X-RAY BINARIES

OBSERVED WITH ASTROSAT

By

VANZARMAWII

Department of PHYSICS

Supervisor: Dr. LALTHAKIMI ZADENG

Co-Supervisor: Prof. RANJEEV MISRA

Submitted

In partial fulfillment of the requirement of the Degree of Doctor of Philosophy in

Physics of Mizoram University, Aizawl



Mizoram University (A Central University)

Tanhrih-796 004, Aizawl, Mizoram

Department of Physics

(DST-FIST Supported Department)

Dr. Lalthakimi Zadeng

Associate Professor

Ph.: +91-9436152904

Email: kimizadeng@gmail.com

Post Box No. 190

Gram: MZU

Phone: 0389-2330435, 230522

CERTIFICATE

This is to certify that the thesis entitled “Spectral Timing Studies of X-ray Binaries Observed with AstroSat” submitted by Ms. Vanzarmawii (Registration No: MZU/Ph. D./1263 of 16.08.2018) for the degree of Doctor of Philosophy (Ph. D.) of the Mizoram University, embodies the record of original investigation carried out by her under my supervision. She has been duly registered and the thesis presented is worthy of being considered for the award of the Ph. D. degree. This work has not been submitted for any degree of any other universities.

(Dr. LALTHAKIMI ZADENG)

Supervisor

(Prof. RANJEEV MISRA)

Jt. Supervisor

MIZORAM UNIVERSITY

TANHRIL

Month: April

Year: 2024

DECLARATION

I, Vanzarmawii, hereby declare that the subject matter of this thesis entitled “Spectral Timing Studies of X-ray Binaries Observed with AstroSat” is the record of work done by me, that the contents of this thesis did not form basis of the award of any previous degree to me or to the best of my knowledge to anybody else, and that the thesis has not been submitted by me for any research degree in other University/Institute.

This is being submitted to the Mizoram University for the degree of Doctor of Philosophy (Ph. D.) in Physics.

(VANZARMAWII)

Candidate

(Dr. LALTHAKIMI ZADENG)

Supervisor

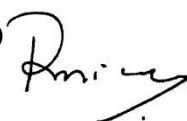
(Prof. ZAITHANZAUVA)

Head of Department

(Prof. RANJEEV MISRA)

Jt. Supervisor

IUCAA



ACKNOWLEDGEMENT

Foremost, I would like to express my sincere gratitude to my supervisor, Dr. Lalthakimi Zadeng, Associate Professor, Department of Physics, Mizoram University, Aizawl, for her valuable guidance and supervision throughout the course of my work.

I would also like to express my heartfelt gratitude to my Joint Supervisor, Prof. Ranjeev Misra, Inter-University Centre for Astronomy and Astrophysics (IUCAA), Pune, who introduced me to data analysis and for guiding me through every step of the way despite the long distance and for always being a good host whenever I am at IUCAA.

I would also like to acknowledge Professor Suman Rai, Department of Physics and Dean, School of Physical Sciences, Mizoram University, Aizawl for his support in the completion of my work. I extend my gratitude to Prof. Zaithanzauva Pachuau, Head of Department, Department of Physics and all the Faculties of the Department of Physics, Mizoram University for their helpful co-operation, timely suggestions and valuable opinions.

I owe a lot to the Post-Doctoral Fellows of IUCAA who taught me primary data analysis techniques specially, Dr. Savithri Ezhikode and Dr. Bari Maqbool. I am also truly grateful to Dr. Jayashree Roy, IUCAA, who spare her time in overseeing my work and providing me with her valuable knowledge.

I also wish to express my heartfelt thanks to my friends, Mr. Lalbiaktluanga, Mr. Samuel Lalsawmliana Lawitlang and Mr. H. Lalthantluanga for their friendship, encouragement and delightful company as we traverse together through tough waters. I am also truly grateful to my fellow Research Scholars, Department of Physics, Mizoram University for their support and insightful knowledge during the course of my work.

In these five years of my Ph.D, I have learned a lot academically and personally. I therefore take this opportunity to thank every single person who was a part of my Ph.D journey. Thank you for believing in me.

I am forever indebted to my parents and siblings for their encouragement and moral support. Above all else, I thank God for being with me all these years and for the health and guidance he bestowed upon me all through the completion of my research work.

Dated: April, 2024

Place: Aizawl

(VANZARMAWII)

Contents

Certificate	i
Declaration	ii
Acknowledgement	iii
List of Figures	vi
List of Tables	x
1 Introduction	1
1.1 Review of Literature	3
1.2 X-ray Binaries	9
1.3 Accretion and Eddington Limit	12
1.4 Binary evolution	13
1.4.1 Roche-lobe overflow	14
1.5 Neutron Star X-ray Binaries	15
1.6 Quasi-periodic Oscillations	17
2 Instruments	21
2.1 AstroSat	22
2.1.1 SXT	23
2.1.2 LAXPC	25
2.2 Data Reduction	25
2.2.1 SXT	26
2.2.2 LAXPC	26
2.3 Data Analysis Technique	27
2.3.1 Timing Analysis	27
2.3.2 Spectral Analysis	28

3	Detection of QPO in the source	30
3.1	Neutron Star Low-mass X-ray Binary Source Cygnus X-2	31
3.2	Observation and Data Analysis	33
3.2.1	Spectral Analysis	34
3.2.2	Timing Analysis	37
3.3	Results and Discussion	40
4	Spectral behaviour of Cygnus X-2 along the Z-track	43
4.1	Z-type sources of Neutron Star Low-mass X-ray Binary	44
4.2	Observations and Data Reduction	46
4.2.1	Spectral Analysis	46
4.3	Results and Discussion	62
4.4	Conclusions	64
5	Summary and Conclusions	66
	Bibliography	70
	Bio-data of the Candidate	82
	List of conferences	84
	Publications	86
	Particulars of the Candidate	88

List of Figures

1.1	Classification of XRBs.	10
1.2	Typical HMXBs and LMXBs have accretion stars that are neutron stars (Tauris & van den Heuvel, 2006). In LMXBs, neutron stars absorb matters via an accretion plate formed by accretion currents of Roche Lobe overflow that also passes through Lagrangian point L_1 , whereas in HMXBs, neutron stars' accretion matters are provided by strong stellar winds or Roche Lobe overflow that passes through Lagrangian point L_1	11
1.3	For a given mass ratio, the equipotential surfaces of a binary system are presented. M_1 and M_2 are the masses of the binary system's stars. The L_1 point is used for mass transfer from the companion to the compact item. Kuster, 2004 contributed to this image.	13
1.4	RXTE/PCA data created spectral branches of NSs. (a) CCD of the 4U 1608-52 atoll source; (b) Color-color diagram of the GX 9 + 1 atoll source; and (c) HID of the Z source GX 340 + 0. Soft colour is defined as 3.5 - 6/2 - 3.5 keV, harsh colour is defined as 9.7 - 16/6 - 9.7 keV, and intensity is defined as 2 - 16 keV, all normalised to Crab (van der Klis, 2006).	18
2.1	An artistic image of AstroSat. Pic Credit: ISRO	23
2.2	Above: Mirror assembly of SXT. Below: 3 units of LAXPC instrument at the time of integration. Pic Credit: ISRO	24

3.1	X-ray hardness intensity diagram of Cyg X-2. The horizontal branch of the Z pattern is seen. Black circles represents the overlapping time of observation of LAXPC and SXT. The open red square represents data sets where only LAXPC data available. The duration of the non-overlapping data set is 4892.9 sec.	35
3.2	Spectra of LAXPC and SXT fitted with a model consisting of Comptonizing corona and disk emission with interstellar absorption with best fit parameters listed in Table 3.1. The black and red data points represent the LAXPC20 and SXT data respectively.	36
3.3	Power density spectrum of LAXPC from a single observation of Cyg X-2 in the 4.0-30.0 keV fitted with three Lorentzians and a power law.	39
3.4	Power density spectra of LAXPC from a single observation of Cyg X-2 in the 4.0-6.0 keV (circle), 6.0-10.0 keV (box) and 10.0-30.0 keV (star) all fitted with three Lorentzians and a single powerlaw.	39
3.5	Time lag (top) and fractional r.m.s (bottom) and as a function of photon energy. For time-lag vs energy (top) the black denotes the ~ 10 Hz while red denotes the ~ 42 Hz. The black denotes the ~ 42 Hz while red denotes the ~ 10 Hz QPOs for the r.m.s vs energy (bottom).	40
4.1	HID of Observation 9000000348 with horizontal branches- HB1, HB2 and HB3	48
4.2	LAXPC and SXT spectra of Obs 9000000348 in the region HB1 shown in Fig.4.1. Here the red lines denote SXT and the black line denotes LAXPC. The same color schematic is used for all figures of the LAXPC and SXT spectra.	48
4.3	LAXPC and SXT spectra of Obs 9000000348 in the region HB2 shown in Fig.4.1	49
4.4	LAXPC and SXT spectra of Obs 9000000348 in the region HB3 shown in Fig.4.1	49

4.5	HID of Observation 9000003206 with different branches. From the bottom right, we have the flaring branches denoted by, FB1 and FB2. Then we have the softapex in the middle section followed by the normal branches, NB1 and NB2 on the upper right.	50
4.6	Spectra of LAXPC and SXT for Obs 9000003206 in the region FB1 shown in Fig.4.5	51
4.7	Spectra of LAXPC and SXT for Obs 9000003206 in the region FB2 shown in Fig.4.5	51
4.8	Spectra of LAXPC and SXT for Obs 9000003206 in the region Softapex shown in Fig.4.5	52
4.9	Spectra of LAXPC and SXT for Obs 9000003206 in the region NB1 shown in Fig.4.5	52
4.10	Spectra of LAXPC and SXT for Obs 9000003206 in the region NB2 shown in Fig.4.5	53
4.11	HID of Observation 9000003064 with different branches. From the right we have the hardapex, followed by the normal branches NB2 and NB1 as we move towards the left.	54
4.12	Spectra of LAXPC and SXT for Obs 9000003064 in the region NB1 shown in Fig.4.11	54
4.13	Spectra of LAXPC and SXT for Obs 9000003064 in the region NB2 shown in Fig.4.12	55
4.14	Spectra of LAXPC and SXT for Obs 9000003064 in the region Hardapex shown in Fig.4.11	55
4.15	HID of Observation 9000002982 with different branches. Starting from the bottom we have a single flaring branch, FB, followed by the softapex. Moving upwards we can see the normal branches denoted by NB1, NB2 and NB3.	56

4.16 Spectra of LAXPC and SXT for Obs 9000002982 in the region FB shown in Fig.4.15	57
4.17 Spectra of LAXPC and SXT for Obs 9000002982 in the region Softapex shown in Fig.4.15	57
4.18 Spectra of LAXPC and SXT for Obs 9000002982 in the region NB1 shown in Fig.4.15	58
4.19 Spectra of LAXPC and SXT for Obs 9000002982 in the region NB2 shown in Fig.4.15	58
4.20 LAXPC and SXT spectra of Obs 9000002982 in the region NB3 shown in Fig.4.15	59
4.21 HID of Observation 9000002130 with different branches. From the right we have the flaring branches FB2 and FB1 moving towards the softapex. .	60
4.22 LAXPC and SXT spectra of Obs 9000002130 in the region NB1 shown in Fig.4.21	60
4.23 LAXPC and SXT spectra of Obs 9000002130 in the region NB2 shown in Fig.4.21	61
4.24 LAXPC and SXT spectra of Obs 9000002130 in the region NB3 shown in Fig.4.21	61

List of Tables

3.1	X-ray Spectral Parameters of ObsID:9000000348 of Cyg X-2	37
3.2	Power Density Spectral Parameters for a single observation of Cyg X-2 . .	38
4.1	X-ray Spectral Parameters of ObsID:9000000348 using models tbabs (Wilms <i>et al.</i> , 2000), gaussian, thcomp (Zdziarski <i>et al.</i> , 2020) and diskbb (Mit- suda <i>et al.</i> , 1984)	50
4.2	X-ray Spectral Parameters of ObsID:90000003206 using models tbabs (Wilms <i>et al.</i> , 2000), gaussian, thcomp (Zdziarski <i>et al.</i> , 2020) and diskbb (Mit- suda <i>et al.</i> , 1984)	53
4.3	X-ray Spectral Parameters of ObsID:90000003064 using models tbabs (Wilms <i>et al.</i> , 2000), gaussian, thcomp (Zdziarski <i>et al.</i> , 2020) and diskbb (Mit- suda <i>et al.</i> , 1984)	56
4.4	X-ray Spectral Parameters of ObsID:90000002982 using models tbabs (Wilms <i>et al.</i> , 2000), gaussian, thcomp (Zdziarski <i>et al.</i> , 2020) and diskbb (Mit- suda <i>et al.</i> , 1984)	59
4.5	X-ray Spectral Parameters of ObsID:90000002130 using models tbabs (Wilms <i>et al.</i> , 2000), gaussian, thcomp (Zdziarski <i>et al.</i> , 2020) and diskbb (Mit- suda <i>et al.</i> , 1984)	62

Chapter 1

Introduction

The early flights of repurposed military rockets were the first to detect and study the X-ray emission from the Sun's corona; this was the first incident of X-ray astronomy. In 1962, a team headed by Riccardo Giacconi at American Science and Engineering detected the first sources beyond the solar system during a rocket flight. Geiger counters were used by the rocket, which had a system designed to cut down the non-X-ray background and collimators, which limit the area of sky visible to the counters. The brightest non-solar X-ray source, later called Scorpius X-1 (Sco X-1), happened to pass over the field of view (FOV) of the rocket as it rotated (Giacconi *et al.*, 1962). Additional research revealed that Sco X-1 was ten thousand times brighter than the Sun. A uniform background glow was also detected, which was unresolvable into individual sources. Further study identified that Sco X-1 was an interacting binary having a compact (neutron star) binary, and this counterpart of Sco X-1 was eventually discovered to be a fainter star of 13 magnitude, which perplexed scientists as to the reason for the source's X-ray emission. This experiment detected extraterrestrial X-ray emission, which led to the birth of X-ray astronomy. Based on these dazzling results, the concept of mass accretion onto the compact object was proposed as a possible explanation for the occurrence of high-energy emission from extra-solar sources.

This success prompted various variety of groups to conduct additional suborbital rocket flights. More X-ray binaries, as well as X-ray emission from supernova remnants, radio galaxies M87 and Cygnus-A, and the Coma cluster, were detected. Geiger counters were replaced with proportional counters, which supplied information on the energy spectra of the sources. Because only collimators were available, finding precise placements of sources was a persistent difficulty.

Giacconi's team created the first X-ray astronomy satellite, Uhuru, which was launched by NASA in 1970. It surpassed the combined observation time of all prior X-ray astronomy experiments on its first day. Uhuru used collimated proportional counters to conduct an all-sky scan, detecting over 300 unique sources, and supplied the first catalogue of the high-energy sky (Forman *et al.*, 1978). Pulsations from X-ray binaries and prolonged

X-ray emission from galaxy clusters were among the discoveries made by Uhuru.

The Einstein Observatory, founded in 1979 to commemorate the centenary of Einstein's birth, was responsible for the next revolution in X-ray astronomy. Although X-ray focusing optics had been flown on Copernicus and as part of Skylab's Solar Astronomy experiment, the Einstein Observatory delivered the first X-ray photographs of several types of astronomical objects. Several X-ray observatories, including EXOSAT, Ginga, ASCA, RXTE, BeppoSAX, and Suzaku, have significantly enriched our understanding of X-ray binary systems as well as other areas of high energy astrophysics, such as studies of Active Galactic Nuclei (AGN), supernova remnants, rotation-powered pulsars, magnetars, and Gamma-Ray Bursts. Dedicated X-ray missions such as the Chandra X-ray Observatory (CXO), XMM-Newton, INTEGRAL, Swift, NuSTAR, and ASTROSAT are active in the sky and producing astounding data on a daily basis.

This thesis is aimed to study the behaviour of an X-ray binary source, Cygnus X-2 (Cyg X-2), through timing and spectral analysis. A portion of the thesis is aimed at the study of Quasi-Periodic Oscillations (QPO) in X-ray binaries, while the rest is aimed at the study of the Z-track in the Cyg X-2 source. The introductory chapter describes an overview of X-ray binaries, mass accretion rate, and Eddington limit as well as the binary evolution.

1.1 Review of Literature

Piraino and his team observed the Z-type low-mass X-ray binary Cyg X-2 using a joint BeppoSAX/RXTE. The source was in the so-called high overall intensity condition and passed through all three branches of the Z track in less than 24 hours. The absorbed total of a soft thermal component, modelled as either a blackbody or a multicolour disc blackbody, and a Comptonized component could be used to characterise the continuum X-ray spectrum. The temporal power spectrum revealed a number of components, including QPOs in the 28-50 Hz band while the source was on the horizontal branch (horizontal

branch oscillation; HBO). They discovered that the HBO frequency was highly associated with the soft thermal component characteristics in the X-ray spectrum (Piraino *et al.*, 2001).

Baluciska-Church and his co-workers proposed an explanation of the Cyg X-2-like Z-track sources. The normal branch is dominated by the neutron star's growing radiation pressure, which is created by an increasing mass accretion rate between the soft and hard apices. The radiation pressure on the horizontal branch continues to rise, becoming several times super-Eddington. They believe that this breaks the inner accretion disc and causes a portion of the accretion flow to be deflected vertically, generating jets that are identified by radio emission in this area of the Z-track. As a result, they claim that significant radiation pressure is required for jet launch. There is a significant rise in neutron star blackbody luminosity on the flaring branch at a constant mass accretion rate, indicating an extra energy source on the neutron star. They discover that there is good agreement between the neutron star's mass accretion rate per unit emission area at the commencement of flaring and the theoretical critical threshold at which burning becomes unstable. As a result, they hypothesise that flaring in Cyg X-2-like sources is caused by unstable nuclear burning. Correlation of kilohertz QPO frequency measurements in all three sources with spectral fitting results leads to the proposal that the upper kHz QPO is an oscillation that always occurs at the inner accretion disc edge, the radius of which increases due to disruption of the disc by the neutron star's high radiation pressure (Baluciska-Church *et al.*, 2010).

Using the data obtained with the Rossi X-ray Timing Explorer (RXTE), Wijnands and others reported the discovery of a 5 Hz QPO in Cyg X-2, a bright low-mass X-ray binary and Z source, at high overall intensities (the high-intensity state). This QPO was discovered on the so-called normal branch and may be distinguished from the normal-branch QPO or NBO. Their identification of the NBO was the first during the high-intensity state of Cyg X-2. This QPO's rms amplitude reduced from 2.8 per cent between 2 and 3.1 keV to 1.9 per cent between 5.0 and 6.5 keV. Its amplitude rapidly grew over 6.5 keV, reaching

12 percent rms above 16 keV. The QPO time lags were consistent with being zero below 5 keV (relative to the 2-3.1 keV band), but they rapidly grew to 70 ms (140) at about 10 keV, after which the time delays were nearly constant near 70 ms. The photon energy dependences of the rms amplitude and time lags for the NBO with other satellites (Ginga, EXOSAT) at other (i.e., lower) intensity states are remarkably similar (Wijnands *et al.*, 2001).

Kuulkers and van der Klis reported the detection of 26 Hz QPO during an 800 s intensity decrease in the flaring branch state of the low-mass X-ray binary Cyg X-2. The QPOs differ from flare branch QPO reported in other “Z” sources, which are frequently attributed to oscillations in a radial flow of matter. The presence of 26 Hz QPO during a dip suggests that they occur in a material that partially obscures the X-ray emission. They explain the novel QPOs phenomenon using a model that includes radial flow and a thick, torus-like inner disc (Kuulkers and van der Klis, 1995).

Kuznetsov, 2002 reported Cyg X-2 RXTE observations from 1996 to 1999. The properties of QPOs are thoroughly examined. To find kHz QPOs, a new method of averaging the power-density spectra collected during several observations is applied. Its distinguishing feature is the grouping of observations not only by the spectrum properties of the source’s X-ray emission but also by their temporal properties. The acquired results are used for an investigation of a slowly spinning neutron star using the transition-layer model (TLM) and the relativistic-precession model (RPM). The two models’ theoretical predictions are compared, and their self-consistency is confirmed. These models are used to calculate the magnetosphere’s tilt to the accretion-disc plane, as well as the neutron-star mass and angular momentum. Observational data is used to calculate the distance to the source (Kuznetsov, 2002).

Using EXOSAT data, Kuulkers and his team examined the X-ray spectrum fluctuations of the low-mass X-ray binary Cyg X-2 over time scales greater than one day. These differences are described in terms of shifts and shape modifications of the “Z” pattern in X-ray color-color diagram and hardness-intensity diagrams. Cyg X-2 has three intensity

“levels”: “high”, “medium”, and “low”. The Z pattern is more intense overall during the high-level episode than it was during the medium-level episode. The shape of the Z pattern also differs between the high and medium levels. Both the color-color diagram and the hardness intensity diagram (HID) reveal a visible flaring branch during the medium level episode. The intensity decreases while the colours increase at the upper half of this episode’s flaring branch (‘color-dependent dip’). A branch is visible in the hardness-intensity diagram but not in the color-color diagram during one of the high level occurrences, which we interpret as flaring branch behaviour. The intensity decreases in this branch but the colours remain constant (a ‘color-independent dip’). During a low level incident, when the source had the lowest overall intensity compared to all other observations, there was no Z shape but only one broad, curved branch due to flares on time scales of 300-500 s, which are larger at high energy. This behaviour has previously been observed in data from other satellites. They find that a total of six high, eleven medium, and three low-level events with appropriate colour data were recorded. More than six low-level incidents occurred in total. All of the low-level events occurred between orbital phases 0.8 and 0.2 (where phase 0.0 represents the X-ray source superior conjunction), implying that the view of the inner disc was partially occluded, possibly by the secondary or mass transfer stream. They attribute the presence of the high, medium, and low intensity levels to a system component that frequently obscures (part of) the emission regions and claim that it is only visible in sources with high inclinations. They look into whether the appearance of the three levels is periodic, as one would expect from a precessing disc (Kuulkers *et al.*, 1996).

In the work carried out by Kuulkers and his co-workers, RXTE PCA observations of Cyg X-2 were recorded in October, 1996 and September, 1997, when its total intensity was approaching its lowest values. For the first time, they investigate fast timing behaviour at such low intensities. The source was most likely in the lower portions of the normal branch and flare branch during the October, 1996 observations and in the lower parts of the horizontal branch during the September, 1997 observations. They discover that the

features of the very low-frequency noise observed in September 1997 are consistent with a monotonic reduction in its strength and power-law index as a function of total intensity. The power of the ~ 6 Hz normal branch QPOs, on the other hand, does not vary monotonically with overall intensity. They are strongest when the overall intensity is medium and weaker when the overall intensity is low or high (Kuulkers *et al.*, 1999).

Wijnands and others evaluated all X-ray data from Ginga’s low-mass X-ray binary Cyg X-2. The examination of the spectrum and fast timing behaviour of these four years of data revealed new insights about the Z source’s behaviour. They validated previously observed recurring patterns of behaviour in X-ray color-color and HIDs, which consisted of shifts and shape changes in the Z track. The behaviour of the source is connected to the overall intensity. When the overall intensity rises, so does the mean velocity of motion along the Z track’s normal branch (NB), as well as the breadth of the NB in the HID. In contrast to earlier findings, they find that while the source is at the same position in the NB of the Z track during different observations, the fast X-ray variability varies dramatically. A normal branch QPO was found at the Kuulkers *et al.* (1996) “medium” overall intensity level, but not during the “high” overall intensity level. The very-low frequency noise component on the lower NB is very strong during the high overall intensity level episodes, whereas it is significantly weaker during the medium overall intensity level events. It is difficult to reconcile the differing overall intensity levels with a precessing accretion disc with our results. Furthermore, as Cyg X-2 enters the upper NB, the frequency of the horizontal branch QPO falls, yielding an upper limit on the magnetic field strength at the magnetic equator of 8.5×10^9 G. They also report five 5-second bursts whose occurrence is unrelated to Z track location, overall intensity level, or orbital phase. They are not ordinary type I bursts, according to the burst properties (Wijnands *et al.*, 1997).

Di Salvo and his team presented the results of a broadband (0.1-200 keV) spectrum investigation of Cyg X-2 conducted with two BeppoSAX observations in 1996 and 1997, for a total effective on-source time of 100 ks. During the 1996 and 1997 observations, the source was in the HB and the NB, according to the color-color diagram and HID.

Five spectra were chosen in the color-color diagram/HID around different positions of the source, two in the HB, and three in the NB. These spectra are fitted to a model that includes a disc blackbody, a Comptonization component, and two Gaussian emission lines at ~ 1 and ~ 6.6 keV. The addition of a hard power-law tail with photon index ~ 2 that contributes $\sim 1.5\%$ of the source brightness enhances the HB spectral match. The soft component is interpreted as emission from the inner accretion disc, with an inner temperature, kT_{in} , fluctuating between ~ 0.8 and ~ 1.7 keV and an inner radius, R_{in} , varying between ~ 26 and ~ 11 km (assuming a system inclination angle of 60°). The Comptonization component is most likely generated by hot plasma surrounding the NS (electron temperature kT_e ranging between ~ 3 and ~ 20 keV, optical depth $\tau \sim 110.4$, seed-photon temperature $kT_W \sim 12.4$ keV). The changes in the blackbody component values imply that as the source goes from the HB to the NB, the inner rim of the disc approaches the Neutron Star (NS) surface, i.e., as the (inferred) mass accretion rate increases. When the source travels from the HB to the NB, the characteristics of the Comptonized component change dramatically as well (Di Salvo *et al.*, 2002).

Smale presented the results of a high-intensity RXTE Proportional Counter Array (PCA) observation of Cyg X-2, during which the source crossed across the normal and horizontal branches of its Z diagram and mapped out a fresh, significant upturn on the HB. A strong X-ray burst was seen during this upturn condition, with rise and decay durations of ~ 1 and ~ 5 s, respectively, and a peak flux of $1.52 \times 10^8 \text{ erg cm}^{-2} \text{ s}^{-1}$. The energy-dependent profile, energetics, and spectral development all point to this being a type I X-ray burst, with evidence for photospheric radius expansion in the first 2 seconds and spectral cooling later on. The discovery of these events resolves the earlier ambiguity regarding the nature of Cyg X-2 bursts and allows us to establish an independent determination of the source distance of 11.6 ± 0.3 kpc (Smale, 1998).

1.2 X-ray Binaries

X-ray binaries (XRBs) are a class of binary stars, so-called because they emit X-rays. They are the most luminous galactic X-ray source, with luminosities ranging from $10^{33} \text{ erg s}^{-1}$ - $10^{38} \text{ erg s}^{-1}$. The binary star comprises of a companion star and an accretor. These X-rays are produced by matter falling from the donor star to the accretor. The donors are usually normal stars, and accretors are collapsed stars that are very compact, e.g., neutron stars (NS), white dwarfs (WD), or black holes (BH). Depending on the type and evolutionary state of the companion star, mass accretion can occur by a variety of processes, including Roche-lobe overflow, stellar wind capture, and Be-disc accretion. The measured X-ray emission qualities are essentially influenced by the nature of the compact object. If the accreting object is a neutron star, its powerful magnetic field (10^{12} G) truncates the accretion flow and concentrates matter onto its magnetic poles at several hundred neutron star radii. At the poles, a thermal mound forms, which serves as a primary source of X-ray emission. In the case of a low magnetic field neutron star, an accretion disc that extends closer to the neutron star's surface is expected to form during the accretion process. High-energy radiation is emitted by the boundary layer between the neutron star and the accretion disc.

The X-ray binaries are classified into two classes according to the masses of the companion star:

- **Low-Mass X-ray Binary (LMXB):** The mass-losing stars in LMXBs have a mass of roughly $1 M_{\odot}$. They are late-type stars, appearing after A-type. They don't have a powerful stellar wind. They fill their Roche lobe, and mass transfer occurs as a result of matter accretion through the inner Lagrangian point caused by Roche lobe overflow. Because the neutron star in the system has a relatively low magnetic field of roughly 10^7 to 10^9 G , accreted matter does not fall onto the magnetic poles. LMXB systems feature a distinct accretion disc, and the majority of X-rays are

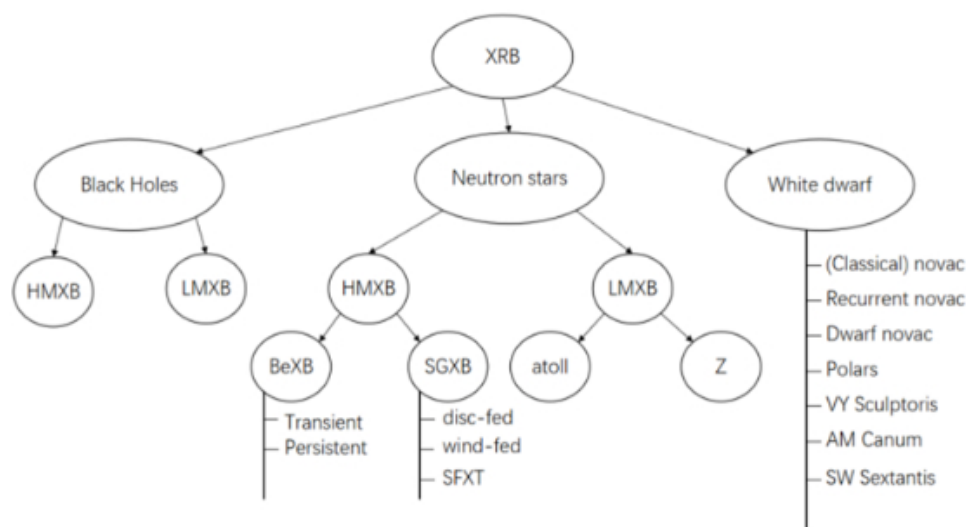


Figure 1.1: Classification of XRBs.

produced near the disc's core and on the neutron star's surface. The accretion disc corona is an extended zone both above and below the disc that produces X-rays. The expanded corona is created by wind material blown off the disc. The heated plasma in the disc scatters X-rays from the corona. Examples are 4U 1820-20, GX 349+2, etc.

- **High-Mass X-ray Binary (HMXB):** The mass-losing star is an early type O or B star with a mass of $10M_{\odot}$. The companion star has a powerful stellar wind that causes the majority of its mass to be lost. In these situations, mass transfer occurs by the compact object's intense accretion of a portion of the matter from the stellar wind of the mass-losing star. Because mass transfer occurs through the capture of matter from the stellar wind, HMXB systems lack a recognisable accretion disc. In HMXBs, the compact object could be a neutron star or a black hole. In these settings, neutron stars have a very strong magnetic field of the order of 10^{12} G. The matter accreted from the companion star's stellar wind is funnelled onto the neutron star's poles along the lines of the magnetic field, resulting in tremendous X-ray emission from the neutron star's poles. Examples are Cen X-3, Vela X-1, etc.

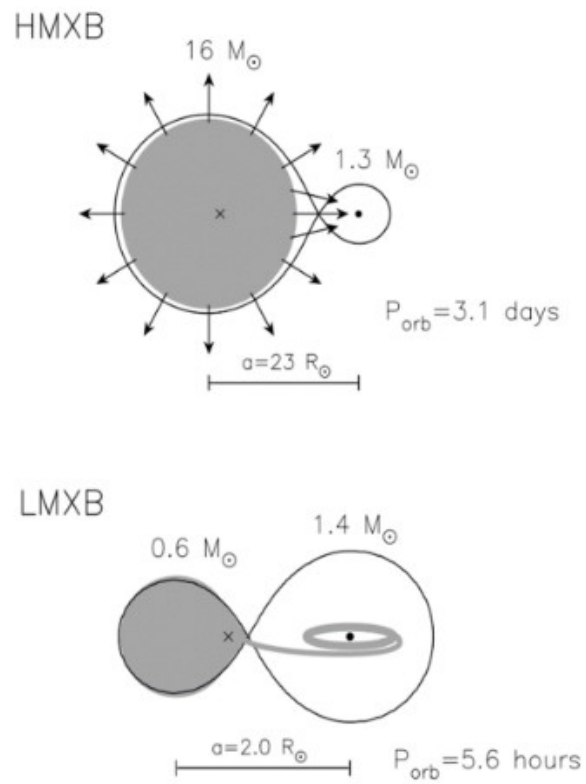


Figure 1.2: Typical HMXBs and LMXBs have accretion stars that are neutron stars (Tauris & van den Heuvel, 2006). In LMXBs, neutron stars absorb matters via an accretion plate formed by accretion currents of Roche Lobe overflow that also passes through Lagrangian point L_1 , whereas in HMXBs, neutron stars' accretion matters are provided by strong stellar winds or Roche Lobe overflow that passes through Lagrangian point L_1 .

1.3 Accretion and Eddington Limit

Mass accretion is the most efficient mode of high energy emission in XRBs and can explain X-ray source data (Zeldovich & Guseynov, 1966). It converts accreting matter's gravitational potential energy into kinetic energy. A simple calculation can demonstrate the effectiveness of the accretion mechanism. Assume a particle of mass, m travelling from infinity to a compact object of mass M and radius R . The amount of energy emitted during this process can be calculated as,

$$E_{acc} = \frac{GMm}{R}$$

here, G is the gravitational constant. According to this equation, the efficacy of accretion as an energy release process is clearly reliant on the compactness of the accreting item. The accretion of 1 gm of matter provides an immense amount of energy $E_{acc} \sim 10^{20}$ erg for a typical neutron star with $M=1.4 M_{\odot}$ and $R=10$ km. This is 20 times more energy than nuclear fusion of hydrogen to helium, which produces $E_{nucl} \sim 610^{18}$ erg (Frank *et al.*, 1992). The accretion energy is determined by the compact object's M/R ratio. As a result, the process of accretion onto neutron stars and black holes is thought to be the most efficient source of energy, with efficiency factors of up to 15% and 40%, respectively. The luminosity generated during this process is referred to as accretion luminosity, which is described as

$$L_{acc} = \frac{GM\dot{m}}{R}$$

The accretion brightness for a given compact object is proportional to the mass accretion rate. It means that the accretion luminosity increases with increasing accretion rate. However, there is a maximum accretion luminosity that an accreting object can achieve. This limiting luminosity is referred to as the Eddington luminosity L_{Edd} . To put it another way, the Eddington luminosity is the limiting luminosity at which gravitational and radiation forces acting on an electron-proton pair are in equilibrium. The expression for Eddington luminosity is as follows:

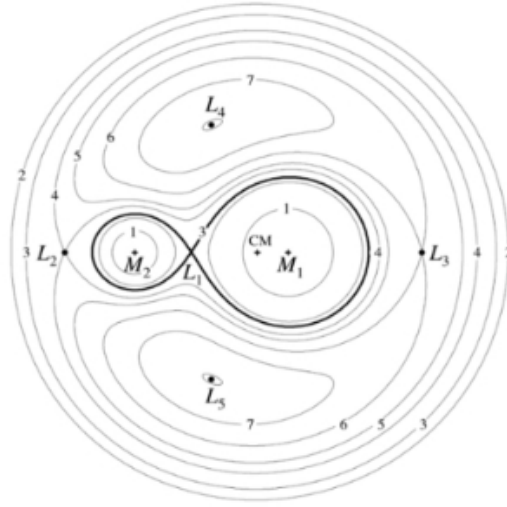


Figure 1.3: For a given mass ratio, the equipotential surfaces of a binary system are presented. M_1 and M_2 are the masses of the binary system's stars. The L_1 point is used for mass transfer from the companion to the compact item. Kuster, 2004 contributed to this image.

$$L_{acc} = \frac{4\pi G m_p c}{\sigma_T} \approx 1.3 \times 10^{38} \frac{M}{M_\odot} \text{ergs}^{-1}$$

where m_p is the proton mass and σ_T is the cross-section of Thomson scattering ($\sigma_T = 6.6 \times 10^{-25} \text{cm}^2$). This formula is based on spherical geometry and steady-flow accretion. However, in cases of non-spherical geometry and non-steady accretion, such as supernova explosions, a compact object's luminosity can exceed the Eddington luminosity. The main origin of X-ray emission is thought to be matter accretion from the companion star to the compact object.

1.4 Binary evolution

We must first understand geometry of the gravitational potential surfaces of both stars in a binary to comprehend the process of accretion mechanism. A star of a specific mass and radius is surrounded by spherical equipotential surfaces. The equipotential surfaces of a star no longer appear symmetric in the presence of a second star. They deviate from spherical geometry and are represented by the Roche potential, which is the combined effective potential of both stars. The Roche potential is represented by

$$\phi_R = -\frac{GM_1}{|r-r_1|} - \frac{GM_2}{|r-r_2|} - \frac{1}{2}(\omega \wedge r)^2$$

where M_1 and M_2 are the masses of two stars, and r_1 and r_2 are the star centre position vectors. The first two terms in the expression represent the possibility of individual stars acting on a test particle at r . The third term denotes the centrifugal potential due to binary rotation at angular velocity ω . The equation does not account for the contribution of Coriolis force. Figure 1.3 depicts the geometry of the Roche potential for a given mass ratio. The lobes of both stars are joined at a location known as inner Lagrange L_1 or saddle point. Both stars' gravitational forces are equal but in opposite directions at this point. In other words, at a Lagrangian point, a test particle experiences zero gravitational force. A binary system can have up to five Lagrangian points. As illustrated in Figure 1.3, three points L_1 , L_2 , and L_3 are in the binary plane, while the other two locations L_4 and L_5 are perpendicular to the plane. If a star evolves and surpasses its own Roche lobe, the extra mass is no longer bound to the star. Through L_1 point, it can be transferred into the gravitational well of another star (Frank *et al.*, 1992; Longair, 1994). Roche-lobe overflow is a sort of mass transfer process. The sections that follow address the Roche-lobe overflow and other forms of mass transfer processes.

1.4.1 Roche-lobe overflow

In general, there are three ways for matter to be transferred from a companion to a compact object. Besides Roche-lobe overflow, we have the stellar wind accretion and the Be/X-ray binaries. However, these two are mainly for high mass XRBs. So for LMXBs the principal mode of mass accretion is the Roche lobe overflow. The optical partner in these systems is a late-type low-mass star with little stellar wind. Matter from the surface of the optical companion exceeds its own Roche-lobe and falls into the gravitational pull of the compact object via the inner Lagrange point as the optical companion evolves or shrinks. This form of mass transfer is referred to as Roche-lobe overflow. Accreting matter carries a considerable amount of angular momentum due to the spinning of the donor star. As a result, rather than falling directly, the accreted matter begins spiralling

around the compact object in the lowest energy orbit, i.e. circular orbit. Only if the circularization radius (R_{cir}) is bigger than the radius of the accreting item is an accretion disc likely to form around the compact object. The circularization radius is generally specified as,

$$R_{cir} = \frac{J^2}{GM_X}$$

where J denotes specific angular momentum (angular momentum per unit mass) and M_X denotes the compact object's mass (Pringle, 1981). The estimation of the circularization radius can also constrain the maximum size of the disc. In other words, this refers to the distance from the point at which the disc begins to develop. Matter in a circular ring loses angular momentum due to dissipative processes such as collision, shock, and viscosity (Shakura & Sunyaev, 1973; Pringle, 1981). As a result, the orbit shrinks towards a lower circular orbit, and an accretion disc forms around the compact object. The circularization radius of LMXBs can be simply expressed as,

$$R_{cir}^{roche} \simeq 3.5 \times 10^9 M_o^{1/3} P_{hr}^{2/3} \text{ cm}$$

P_{hr} is the orbital period of the binary in hours, and M_o is the mass of the companion star in solar masses (Frank *et al.*, 1992). The circularization radius can be approximated for typical parameters as $R_{cir} > 10^9$ cm. Because the radius of a compact object cannot be more than the radius of a white dwarf ($\sim 10^9$ cm), an accretion disc is expected to emerge during the Roche-lobe overflow phase. When accreted materials comes into contact with the surface of a compact object, X-ray emission occurs.

1.5 Neutron Star X-ray Binaries

Neutron star X-ray binaries are a type of X-ray binary in which the compact object is a neutron star. After stellar evolution, neutron stars are born as the end result of massive stars with masses ranging from $11 M_\odot > M \geq 40 M_\odot$ (Iben, 1991; Lewin *et al.*, 1995). They have a powerful magnetic field of $10^8 - 10^{15}$ G. They are regarded as great candidates for probing the properties of matter under severe settings such as high density,

strong gravity, powerful magnetic fields, and extreme velocity regimes by providing a one-of-a-kind astrophysical laboratory. Regardless of mass transfer processes, accreted matter is impacted by the magnetic field as it approaches the neutron star. According to current theories, a strong magnetic field blocks the accretion flow at a particular radius and channels matter towards the neutron star's magnetic poles.

Low-mass ($< M_{\odot}$) stars, such as late-type main-sequence stars, white dwarfs, or subgiant stars with F-G type spectra, are the companions of NSs in NS/LMXBs. Their galactic distribution is centred on the galactic centre, indicating a somewhat old star population with ages ranging from $(0.5 - 1.5) \times 10^{10}$ years. This NS LMXB can be subdivided into Z-type and Atoll type sources based on X-ray spectral and fast timing behaviour (Hasinger & van der Klis, 1989). Z sources accrete matter at a rate that is a significant fraction of the Eddington critical rate, $0.5 - 1 L_{Edd}$. The Z sources trace out a Z-shape in the Z-ray color-color diagram. The branches of the Z-type sources are the horizontal, normal and flaring branch, being traced from top to bottom. The overall intensity fluctuates smoothly among the branches on time durations ranging from weeks to months. The hard vertex is the transition between the HB and the NB, and the soft vertex is the transition between the NB and the FB. The movement along the Z-track is considered to be caused by fluctuations in the mass transfer rate to the compact object (e.g., Hasinger & van der Klis, 1989; Lamb, 1991; Kuulkers *et al.*, 1996; Wijnands *et al.*, 1997). The Z sources are classified into two groups (Hasinger & van der Klis, 1989; Kuulkers *et al.*, 1997) (i) the Cyg-like sources Cyg X-2, GX 5-1, and GX 340 + 0 where the HB, NB, and FB are seen but with weak flaring and (ii) the Sco-like sources Sco X-1, GX 349 + 2, and GX 17 + 2 where flaring is strong and frequent but with a short or weak HB. Cyg-like sources typically display all three branches of the Z-track, whereas Sco-like sources have a weak HB but a significantly stronger FB (Church *et al.*, 2012). Theoretical investigations (Psaltis *et al.*, 1995) show that Cyg-like sources have higher magnetic fields ($B \sim 5 \times 10^9$ G) than Sco-like sources ($B \sim 10^9$ G). Similarly, from the so-called island state to the upper banana branch, the accretion rate increases in atoll sources.

Cygnus X-2 (Cyg X-2) is a well-studied brilliant low-mass X-ray binary that is categorised as a Z source since it follows a Z-pattern in the X-ray CD (e.g. Hasinger & van der Klis, 1989; Kuulkers *et al.*, 1996). Byram *et al.*, 1966 discovered it with a sounding rocket experiment. Cyg X-2 was originally detected by EXOSAT during a 14-hour period beginning on 23 July 1984, at 02:07 UT, using a gas scintillation proportional counter (Peacock *et al.*, 1981) and one-half of the medium energy detectors (Turner *et al.*, 1981). Cyg X-2's X-ray spectrum has been intensively investigated over the years. BeppoSAX was used to investigate the broad-band X-ray spectrum of this source (Frontiera *et al.*, 1999; Di Salvo *et al.*, 2002; Piraino *et al.*, 2002). The presence of lines from distinct K-shell ions was confirmed by spectral analysis utilising ASCA and BeppoSAX data (Kuulkers *et al.*, 1997; Di Salvo *et al.*, 2002). Cyg X-2, like other brilliant LMXBs, exhibited Fe K emission in its X-ray spectra.

1.6 Quasi-periodic Oscillations

In time series, quasi-periodic oscillations (QPOs) stand out as a finite-width peak in the power density spectrum (PDS) (see Figure 1.4), whose profile is typically represented by a Lorentzian function.

$$P_\nu \propto \frac{A_0 \omega}{(\nu - \nu_0)^2 + (\frac{\omega}{2})^2}$$

where ν_0 is the peak frequency (or centroid frequency), ω is the full width at half maximum (FWHM), and A_0 is the signal's amplitude. A QPO signal is defined by three parameters: centroid frequency ν_0 , quality factor ($Q \equiv \frac{\nu_0}{FWHM} = \frac{\nu_0}{\omega}$), and the fractional root-mean-squared (rms) FWHM ω amplitude. The centroid frequency ν_0 indicates the signal's position. While FWHM ω , which is connected to the coherence time $\tau = \frac{1}{\pi\omega}$, is frequently expressed in terms of quality factor Q , which is a coherence metric. Signals with $Q > 2$ are known as QPOs, whereas those with $Q < 2$ are known as peaked noises. As a function of the source flux, the rms represents a measure of strength that is proportional to the square root of the integrated power of its contribution to the PDS,

$r \propto P^{\frac{1}{2}} = \sqrt{\int P_\nu d\nu}$ and is frequently represented in percentage.

Neutron stars in LMXBs have significant QPO components, and their frequencies exhibit some correlations.

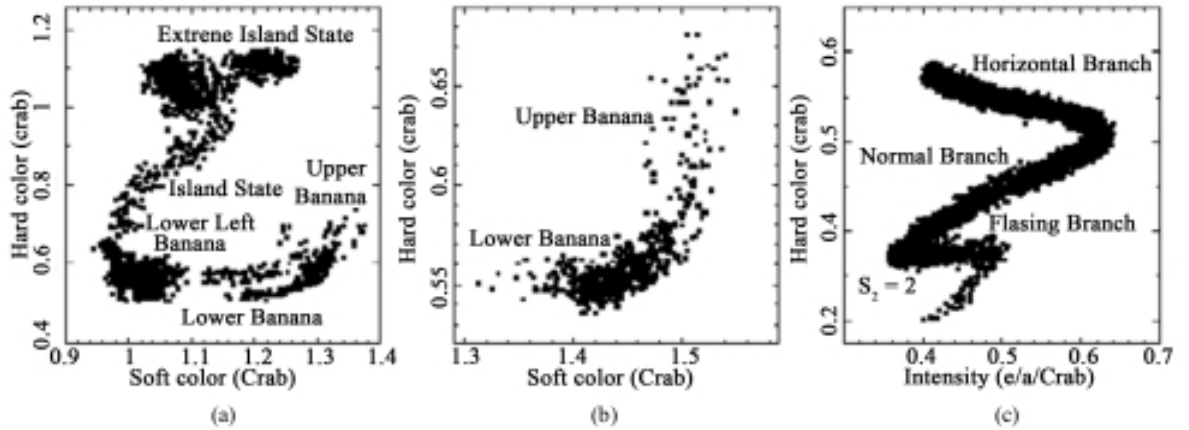


Figure 1.4: RXTE/PCA data created spectral branches of NSs. (a) CCD of the 4U 1608-52 atoll source; (b) Color-color diagram of the GX 9 + 1 atoll source; and (c) HID of the Z source GX 340 + 0. Soft colour is defined as 3.5 - 6/2 - 3.5 keV, harsh colour is defined as 9.7 - 16/6 - 9.7 keV, and intensity is defined as 2 - 16 keV, all normalised to Crab (van der Klis, 2006).

Low-frequency QPOs- Low-frequency QPOs with $Q \leq 2$ and amplitudes of 1% - 10% (van der Klis, 1989) have been seen in the frequency range of 5 - 60 Hz. They are classified as horizontal branch oscillations (HBOs), normal branch oscillations (NBOs), and flaring branch oscillations (FBOs), and correspond with spectral states in NS/LMXB color-color diagrams. HBOs have a characteristic frequency range of ν_{HBO} around 15 - 55 Hz and show a strong positive association with X-ray intensity (van der Klis *et al.*, 1985), for which the magnetospheric beat-frequency model was developed (Alpar & Shaham, 1985). A signal with essentially constant frequency is frequently observed in the middle of NB in a range of about 5 - 7 Hz, with similar coherence and amplitude as HBO. Such NBOs show no clear strong association with X-ray intensity. FBOs have been observed as an intensity-dependent peak in the frequency range of roughly 10 - 20 Hz, merging smoothly with NBOs. As soon as the source turns from NB to FB, the frequency becomes closely associated with X-ray intensity. As the source advances up FB, the peak broadens and eventually collapses into a very broad excess noise component. QPOs from

distinct branches can sometimes arise in the same source at the same time.

Hectohertz QPOs- The hectohertz (hHz) QPO (Ford & van der Klis, 1998) is a peaked noise that is occasionally coherent enough to be referred to as a QPO and has a frequency ν_{Hz} in the range of 100 - 200 Hz (for example see panel (b) in Figure 1.4). It is observed in the majority of states of atoll sources and the millisecond pulsar SAX J1808.4-3658 when the break frequency is ≥ 1 Hz. They could also appear in Z sources. It is distinguished from the other NS components by its nearly constant frequency. The hHz QPO typically has a low quality factor but occasionally peaks at $Q > 2$ and has an rms amplitude of 2% to 20%, becoming weaker and more coherent as the break frequency increases.

Kilohertz QPOs- The kilohertz (kHz) QPOs, which were initially found by the Rossi X-ray Timing Explorer (RXTE) (Bradt *et al.*, 1993) in Scorpius X-1 (van der Klis *et al.*, 1996) and 4U 1728-34 (Strohmayer *et al.*, 1996), respectively, are the fastest variability components in X-ray binaries; for a historical narrative, see van der Klis, 2000, van der Klis *et al.*, 1997. Sometimes just one peak can be seen, but in some sources, the kHz QPOs occur in pairs. In association with source states, the twin peaks move up and down in frequency jointly from 200 Hz to 1300 Hz (van der Klis, 2000). The higher frequency peak in PDS is known as the upper kHz QPO ν_2 , and the lower frequency signal is known as the lower kHz QPO ν_1 . Peaks arise alone around the margins of their reported frequency range. The kHz QPOs are seen in all Z sources and 4U 1728-34 down to the lowest inferred accretion rate \dot{M} levels (HB and upper NB) that these sources attain. At the greatest \dot{M} levels, QPOs are always undetected. QPOs are seen in the section of LLB closest to the islands, i.e. towards the lower left corner of UB, in most atoll sources, and they are frequently not detected in IS, which may be due to low sensitivity at the low count rates there (Mendez *et al.*, 1998).

Frequency correlations of QPOs in NS/LMXB- There are certain relationships between the frequencies of twin kHz QPOs and other components (van der Klis, 2006), which are consistent in Z and atoll sources. HBO frequencies appear to correlate well with kHz QPO frequencies (van der Klis, 1997; Wijnands *et al.*, 1997, Wijnands *et al.*, 1998; Wij-

nands, Mendez, *et al.*, 1998; Jonker *et al.*, 1998, Jonker *et al.*, 2000), and the same is true for NBO in Scorpius X-1 (van der Klis *et al.*, 1996). A systematic study for 0.1 - 1200 Hz QPOs and broad noise components (Psaltis *et al.*, 1999) of non-pulsing NS shows that the frequencies between lower kHz QPOs and low frequency QPOs follow a tight correlation, which can be described by an empirical model based on a superposition of multiple Lorentzians (Belloni *et al.*, 2002). It has been argued that the basis of these correlations is a physical dependency of the frequencies on one another (Stella & Vietri, 1997), and that a combination of the sonic-point and magnetospheric beat-frequency theories can explain these correlations (Psaltis *et al.*, 1999).

Chapter 2

Instruments

To study the bright, persistent neutron star X-ray binary source, we have extracted and analysed the data of AstroSat mission. In this chapter, we will give a brief explanation of the instruments and data reduction as well as data analysis techniques.

2.1 AstroSat

AstroSat is India's first astronomy satellite which was launched on the 28th of September 2015 by Indian Space Research Organisation (ISRO). It is based on Indian Remote Sensing (IRS) spacecraft. It carries an array of instruments which are capable of simultaneous observations in a broad range of wavelengths from the visible, near ultraviolet (NUV), far UV (FUV), soft X-rays to hard X-rays.

AstroSat has five payloads for simultaneous multi-band observations, which are:

- Twin 38-cm Ultraviolet Imaging Telescopes (UVIT) covering Far-UV to optical bands.
- Three units of Large Area Xenon Proportional Counters (LAXPC) covering medium energy X-rays from 3.0 to 80.0 keV with an effective area of 8000 sq.cm. at 10 keV.
- A Soft X-ray Telescope (SXT) with conical foil mirrors and X-ray Charge Couple Device (CCD) detector, covering the energy range 0.3-8.0 keV. The effective area will be about 120 sq.cm. at 1 keV.
- A Cadmium-Zinc-Telluride coded-mask imager (CZTI), covering hard X-rays from 10 to 150 keV, with about 6 deg field of view and 480 sq.cm. effective area.
- A Scanning Sky Monitor (SSM) consisting of three one-dimensional position-sensitive proportional counters with coded masks. The assembly is placed on a rotating platform to scan the available sky once every six hours in order to locate transient X-ray sources.

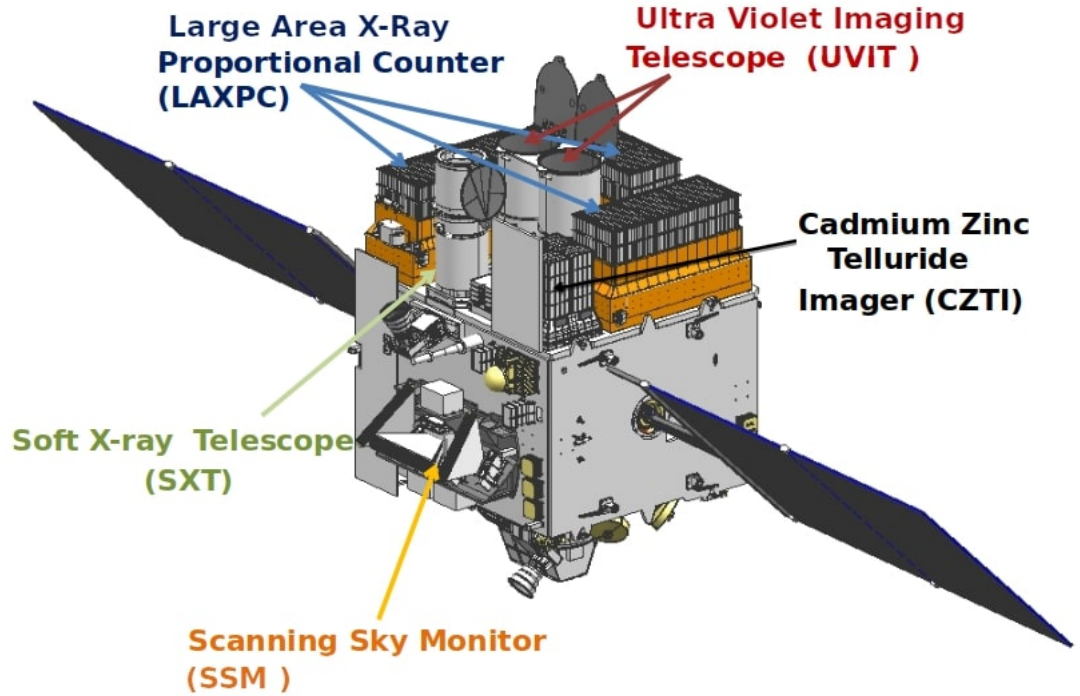


Figure 2.1: An artistic image of AstroSat. Pic Credit: ISRO

The SXT and LAXPC together covers 0.3-80.0keV band in the X-ray sky. In this thesis, we have used SXT and LAXPC observations of LMXB source Cygnus X-2. The working mechanism of the observations are discussed below in detail.

2.1.1 SXT

SXT can perform imaging, spatially resolved spectroscopy, and variability measurements on cosmic sources based on the idea of grazing incidence in a conical approximation of the Wolter I geometry. It is operational in the energy range 0.7-8.0 keV and has an effective area of $\sim 90 \text{ cm}^2$ at 1.5 keV. X-rays are focused on a Charge Coupled Device (CCD-22, produced by E2V Technologies Inc., UK) contained in a Focal Plane Camera Assembly (FPCA). It has a focal length of 2 meters, geometric area of $\sim 250 \text{ cm}^2$, and was designed to have point spread function of $\sim 2\text{-}3$ arc min (FWHM). The field of view (fov) of this instrument is ~ 40 arc min diameter and the pixel size on the CCD is ~ 4

arc sec. The SXT has six data modes: Photon Counting (PC), Photon Counting Window (PCW), Fast Windowed Photon Counting (FW), Bias Map (BM), Calibration (Cal), and House Keeping (HK), however only the PC mode and FW mode are useful for observers. The PC mode has a read-out time of ~ 2.4 s. Meanwhile, in the FW mode 150×150 pixel array window at the centre of the CCD is used with a read-out time of ~ 0.28 s.



Figure 2.2: Above: Mirror assembly of SXT. Below: 3 units of LAXPC instrument at the time of integration. Pic Credit: ISRO

2.1.2 LAXPC

The LAXPC instrument covers 3.0-80.0 keV broad spectral band for studying high time resolution and low spectral resolution of X-ray sources. It is made up of three identical proportional counters i.e, LXP10, LXP20 and LXP30 respectively. Each counter is made up of 60 anode cells measuring $3 \times 3 \times 100$ cm that are arranged in 5 layers to provide a 15 cm deep X-ray detection volume filled with Xenon gas at 2 atm. The combined effective area of these unit are 6000 cm^2 . It has a $0.9^\circ \times 0.9^\circ$ field of view (FOV) defined by a set of collimators. Data can be stored in two modes: i.) Normal (or Default) Modes of Operation and ii.) Fast Counter (FC) Mode.

In Normal operation there are two modes running simultaneously, they are:

- Broad Band Counting Mode Data: It makes a record of the rate of occurrence of events in various energy bands with selectable time bin (16 msec to 2048 msec).
- Event Mode Data: Each event's arrival time is time tagged to an accuracy of 10 microseconds in this mode. At the same time, the energy and identity of each occurrence are recorded. For each accepted and examined event, this mode generates 5 bytes of data. The detector's dead time in this mode is roughly 50 microseconds.

In the FC mode, the event rate is measured only from the top layer of each LAXPC detector in 4 energy channels covering 3-20 keV band with a fixed time bin of 160 microsecond. In this mode dead time is about 10 microsecond. Each of 4 counters are 8 bit deep and cover 3-6, 6-8 , 8-12 and 12-20 keV energy bands. This mode is to be used for studying rapid variability at very high flux.

2.2 Data Reduction

We have downloaded data for both SXT and LAXPC observations from Astrobrowser¹. HEASoft² and its inbuilt tools are also used here for data reduction.

¹https://webapps.issdc.gov.in/astro_archive/archive/Home.jsp

²<https://heasarc.gsfc.nasa.gov/docs/software/heasoft/>

2.2.1 SXT

The SXT level-1 data were processed using SXTPIPELINE³ VERSION AS1SXTLEVEL2-14B released on January 3rd 2019 to generate level-2 data for each orbit. The pipeline provides a Julia code to merge the level-2 SXT data of individual orbits. We have made use of the level-2 data provided in Astrobrowse by the AstroSat team. To avoid pile-up effect of SXT we select an annular region of 1 arcmin inner radius and 8 arcmin outer radius centered on the source to extract the image, light curves and spectra of the source. We have used SKYBKG_COMB_EL3P5_CL_RD16P0_V01.PHA and SXT_PC_MAT_G0TO12.RMF for background and rmf file respectively. Also the SXT arf generation tool SXTARFMODULE was used to generate vignetting corrected arf ARFTESTS1_RAD4P0_VIGCORR.ARF provided by SXT instrument team. The *XSELECT*⁴ utility from the HEASOFT PACKAGE (V 6.26.1) was used to generate the spectra.

2.2.2 LAXPC

Different software has been developed to obtain science products from level-1 data. LaxpcSoft was written in FORTRAN and includes two related pieces of software: the fundamental software, which consists of two FORTRAN programs, laxpcl1 and backshift developed by the TIFR team, and a suite of Fortran programs for various tasks built by the AstroSat Science Support Cell⁵ at IUCAA. LAXPClevel2DataPipeline⁶ was written in C++, and developed with the support from ISRO Space Application Centre (SAC)⁷. The level-1 data include: the Time Calibration Table (TCT) file, the Make Filter (MKF) file, the Low Bitrate Telemetry (LBT) house-keeping file, the orbit file, science data file, Good Time Interval (GTI) and the attitude file. In this thesis, data reduction was performed using LaxpcSoft⁸ software, version as of August 04 2020) to reduce level-1 data to level-2,

³https://www.tifr.res.in/~astrosat_sxt/sxtpipeline.html

⁴<https://heasarc.gsfc.nasa.gov/ftools/xselect/>

⁵<http://astrosat-ssc.iucaa.in/>

⁶https://www.tifr.res.in/~astrosat_laxpc/LAXPC_lv12_pipeline.html

⁷<https://www.sac.gov.in/Vyom/>

⁸<http://astrosat-ssc.iucaa.in/laxpcData>

and standard routines in LaxpcSoft were used to generate light curves, energy spectrum, background files etc. The individual routine for spectra determines the response file. Spectra for both SXT and LAXPC were fitted using XSPEC 12.10.1⁹.

2.3 Data Analysis Technique

In addition to imaging, X-ray detectors are being developed to record the distribution of source photons in time and energy spaces, resulting in the light curve and energy spectrum. The light curve and energy spectrum can be used to study the attributes of a source and the physical mechanisms that induce high energy output. HEASoft package is intended to extract this information through the use of particular tools.

2.3.1 Timing Analysis

Tasks from the XRONOS package are used for timing analysis to look for periodicity or quasi-periodicity in time series data. FTOOLS offers two packages: powspec and efsearch. The powspec job uses the Fourier transform method to build a power density spectra (PDS) in both the power and frequency domains. A high power at a specific frequency indicates the presence of periodicity in data. If the peak in the PDS is relatively weak yet above the continuum and is spread in a Gaussian form, this feature can be interpreted as quasi-periodicity in time series data.

However, Fourier techniques are not the only tools employed in timing analysis, but are one of the most commonly used and are often the starting or comparison point for other analysis.

The Fourier Transform decomposes a signal into a sum of complex exponential (i.e., sinusoidal) components, each with a complex amplitude and a complex phase. The discrete Fourier transform is used when working with discretely sampled, uniformly binned lightcurves. If x_k are the amplitudes of the lightcurve measured at times t_k (subdivided

⁹<https://heasarc.gsfc.nasa.gov/xanadu/xspec/>

into N uniform steps of time bins with width $1/T$), then the discrete Fourier transform is given by,

$$a_j = \sum_k x_k e^{i\omega_j t_k}$$

where, i is imaginary, and ω_j are the discrete Fourier frequencies given by,

$$\omega_j = 2\pi v_j = 2\pi j/T,$$

with j being the integers

$$j = \frac{N}{2} + 1, \dots, \frac{N}{2}.$$

Because we are dealing with actual signals in X-ray astronomy, we normally only deal with positive Fourier frequencies, ω_j , and refer to $2|a_j|$ as the Fourier amplitude and j as the Fourier phase. We will only be dealing with squared Fourier amplitudes, $\alpha a_j^* a_j = |a_j|^2$. The PDS is defined as the sum of these amplitudes vs. frequency. It is a measure of a signal's “power” over a specific frequency range. The PDS, in particular, is a measure of the fractional variability over a specific frequency range. The PDS is frequently expressed in $(RMS)^2/Hz$ units, i.e., (root mean square variability)²/unit frequency.

2.3.2 Spectral Analysis

The goal of spectral analysis is to investigate the form of the energy continuum using various physical models. The Xspec (X-ray Spectral Fitting Package), which is part of HEASoft, allows the fitting of spectra using many models that are included in the package. There are some local models that can be used during the fitting process. Because of the effect of the detector's response and effective area, spectra recorded by a detector do not show the true spectrum of a source. The recorded photon distribution is combined with the detector response to obtain the real source spectrum. The source spectra are fitted in the XSPEC using the χ^2 method with proper background subtraction, response, and effective

area files. In general, the 2 approach, as defined below, tests the difference between data points and models,

$$\chi^2 = \sum \frac{(O-M)^2}{\sigma^2}$$

where O is the observed data and M denotes the model point. σ^2 denotes the variance between data points. The reduced χ^2 , $\chi_{red}^2 = \chi^2/\nu$, is defined as the χ^2 to degree of freedom ratio. The total number of data points minus model parameters equals to the number of degrees of freedom. If the value of χ_{red}^2 equals 1, the model is thought to accurately reflect the observational data acquired from a source. The model is negligible for χ_{red}^2 significantly bigger than one, whereas $\chi_{red}^2 < 1$ relates to a high number of parameters in the model, some of which may not be required or an overestimation of error in the data.

Chapter 3

Detection of QPO in the source

In this chapter we present the analysis of an AstroSat observation of the neutron star low-mass X-ray binary, Cygnus X-2 during the end of February 2016. The hardness-intensity plot obtained using LAXPC data showed that the source was on the horizontal branch of the Z-track and the power density spectrum revealed the presence of a prominent Quasi-periodic Oscillation (QPO) at ~ 42 Hz with broad-band continuum noise at lower frequencies. The large effective area of LAXPC at $\gtrsim 30$ keV, allowed for an unprecedented study of the energy dependence of the ~ 42 QPO and the broad noise continuum at ~ 10 Hz. The fractional r.m.s increases with energy and its shape is similar for both the QPO and the continuum noise suggesting a common radiative origin. However, while the QPO exhibits hard time lags, with the high energy photons lagging the low ones by a few milliseconds, the opposite behaviour is shown by the continuum noise, with the low energy photons lagging the high ones. The wide band photon spectrum from SXT and LAXPC in 0.7-30 keV band, is consistent with a soft component from a disc and a hard Comptonized component from a hot corona. While the energy dependence of the r.m.s shows that both the QPO and the continuum noise variability is dominated by the Comptonized component, the change in sign of the time-lag suggest that the dynamic origin of the QPO may be in the disk while the noise continuum may originate from the corona. In section 3.1 we will describe the source Cygnus X-2 followed by observation and data analysis in section 3.2. Sections 3.3 and 3.4 will contains the results and discussion.

3.1 Neutron Star Low-mass X-ray Binary Source Cygnus X-2

The binary star comprises of a companion star and an accretor. These X-rays are produced by matter falling from the donor star to the accretor. The donors are usually normal stars, and accretors are collapsed stars that are compact, e.g., neutron stars (NS), white dwarf (WD), or black holes (BH). The X-ray binaries are classified into two classes according to the masses of the companion star- high-mass and low-mass X-ray binary. Here

the X-ray binary system comprising a NS as a compact object and a low-mass star as its companion is classified as a neutron star low-mass X-ray binary (NS LMXB). These can be sub-divided into Z-type and Atoll-type sources based on X-ray spectral and fast timing behaviour (Hasinger & van der Klis, 1989). The source- Cygnus X-2 (henceforth Cyg X-2), is a bright, persistent LMXB. It was first observed in the X-rays using the sounding rocket experiment by (Byram *et al.*, 1966). It was then observed by EXOSAT for a continuous duration of 14h starting on July 23rd, 1984, using Gas scintillation proportional counter (Peacock *et al.*, 1981) and one-half of medium energy detectors (Turner *et al.*, 1981).

After the observation of thermonuclear X-ray bursts in Cyg X-2, its compact companion was identified as a NS with a low magnetic field (Kahn & Grindlay, 1984; Smale, 1998), its mass is measured as $M_x > 1.78 \pm 0.23 M_\odot$ (Orosz & Kuulkers, 1999). The binary system has a late-type companion, V1341 Cyg with an orbital period of ~ 9.8 days (Cowley *et al.*, 1979; Casares *et al.*, 1998) and a mass ranging between 0.4 and $0.7 M_\odot$ whose spectral type seem to vary from A5 to F2 (Cowley *et al.*, 1979).

A characteristic feature of these sources is their rapid nearly sinusoidal variation which is revealed by peaks in their power spectra known as Quasi-periodic oscillations (QPO). In the horizontal branch (HB), the frequencies of the QPO vary between $\sim 15\text{Hz}$ to $\sim 55\text{Hz}$ (Alpar & Shaham, 1985; Lamb, 1989; Ghosh & Lamb, 1992), while in the normal branch (NB), the frequencies range between $5\text{--}7\text{ Hz}$ and in the flaring branch (FB), the frequencies are observed to increase from $\sim 6\text{ Hz}$ up to $\sim 20\text{ Hz}$ along the branch (Hasinger, 1990). The sources also exhibit high frequency kHz QPOs, which sometimes occur in pairs (Wijnands *et al.*, 1998; Kuznetsov, 2002). Despite several endeavours to characterise the phenomena, there is at present no consensus on the origin of these different kinds of QPOs.

QPOs as well as broad continuum noise features have been extensively observed in Cyg X-2, by timing studies carried out using the proportional counter array (PCA) onboard the RXTE satellite (Wijnands *et al.*, 1998). Simultaneous detection of twin peaks at 500

and 860 Hz and the highest single kHz QPO at 1007 Hz were reported by (Wijnands *et al.*, 1998). QPO at 18-50 Hz in the HB and 5.6 Hz QPO in the NB were also seen in Cyg X-2 (Elsner *et al.*, 1986; Hasinger *et al.*, 1986; Wijnands *et al.*, 1997; Kuulkers *et al.*, 1999). A 5 Hz QPO was detected in Cyg X-2 by (Norris & Wood, 1986) during an 8 hr observation of the source. The observation carried out by (Kuulkers *et al.*, 1997) showed a similar QPO near ~ 40 Hz in the source.

The LAXPC (Yadav *et al.*, 2016b; Agrawal *et al.*, 2017) instrument onboard the space observatory AstroSat (Agrawal, 2006; Singh *et al.*, 2014) has the advantage over *RXTE* by having a larger effective area at energies $\gtrsim 30$ keV. It has detected high frequency kHz QPO LMXB (Chauhan *et al.*, 2017) at high energies and has shown its ability to provide unprecedented energy dependent timing features (Yadav *et al.*, 2016a; Misra *et al.*, 2017). The SXT instrument (Singh *et al.*, 2016, Singh *et al.*, 2017) onboard provides simultaneous spectral coverage which has allowed for extensive spectro-timing studies of X-ray binaries (Leahy & Chen, 2019; Roy *et al.*, 2020). Here, we report the timing and spectral analysis results of an *AstroSat* observation of Cygnus X-2 during which a ~ 42 Hz QPO was observed.

3.2 Observation and Data Analysis

While a detailed study of the spectral and temporal evolution of Cyg X-2 using all the available *AstroSat* data will be presented elsewhere, here we focus on a single observation (Obs ID 9000000348) undertaken from February 28th 2016 to March 1st 2016 with a start time of 52219.2985s and an exposure time of 64300s for LAXPC and 14290s for SXT. Spectra were fitted using XSPEC PACKAGE, VERSION 12.10.1 (Arnaud, 1996).

The Large Area X-ray Proportional Counter (LAXPC) instrument aboard the *AstroSat* mission covers 3.0-80.0 keV broad spectral band for studying high time resolution and low spectral resolution of X-ray sources (Agrawal, 2006; Antia *et al.*, 2021). The three

LAXPC detectors have a total effective area of about 4500 cm² at 5 keV, 6000 cm² at 10 keV and about 5600 cm² at ~ 40 keV (Roy *et al.*, 2019). Details on the characteristics and calibrations of the LAXPC instruments can be found in (Yadav *et al.*, 2016b; Agrawal *et al.*, 2017; Roy *et al.*, 2016; Antia *et al.*, 2017). Data reduction was performed using LAXPCSOFT software (<http://astrosat-ssc.iucaa.in/laxpcData>, version as of August 04 2020) to reduce level-1 data to level-2, and standard routines in LAXPCSOFT were used to generate light curves, energy spectrum and background files. Since the observations were taken in 2016, we have included data from all the three LAXPC detectors. Later, one of the units, LAXPC 30 developed a gas leak and stopped operating on March 8 2018. The Soft X-ray imaging telescope (SXT) aboard AstroSat has been designed to provide soft X-ray images and spectra in the energy range 0.3-8.0 keV by using conical foil mirrors for X-ray reflection with X-ray Charge Coupled Device (CCD) as the focal plane detector and details of the instrument are given in (Navalgund *et al.*, 2017; Singh *et al.*, 2014). The effective area of SXT is ~ 90 cm² at 1.5 keV. The SXT level-1 data were processed using SXTPIPELINE version AS1SXTLevel2-14b released on January 3rd 2019 to generate level-2 data for each orbit. The pipeline provides a Julia code to merge the level-2 SXT data of individual orbits. To avoid pile-up effect of SXT we select an annular region of 1 arcmin inner radius and 8 arcmin outer radius centered on the source to extract the image, light curves and spectra of the source. We have used Sky-Bkg_comb_EL3p5_Cl_Rd16p0_v01.pha and sxt_pc_mat_g0to12.rmf for background and rmf file respectively. Also the SXT arf generation tool sxtARFModule was used to generate vignetting corrected arf ARFTESTS1_Rad4p0_vigCorr.arf provided by SXT instrument team. The XSELECT utility from the HEASOFT package (v 6.26.1) was used to generate the spectrum.

3.2.1 Spectral Analysis

We have first examined the hardness intensity diagram (HID) constructed using LAXPC lightcurves binned in 100 sec and in the energy ranges 4-8 keV (soft) and 8-10 keV (hard)

as shown in Figure 3.1. The Hardness defined as the ratio of the hard to soft bands does not show significant variation with the total count rate, which suggests that the source is in the Horizontal Branch. Similar variation is seen when different energy ranges are used.

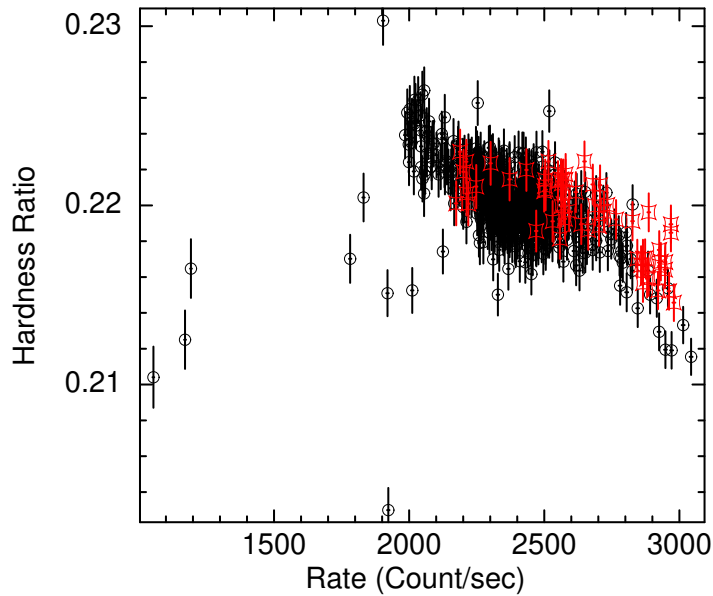


Figure 3.1: X-ray hardness intensity diagram of Cyg X-2. The horizontal branch of the Z pattern is seen. Black circles represents the overlapping time of observation of LAXPC and SXT. The open red square represents data sets where only LAXPC data available. The duration of the non-overlapping data set is 4892.9 sec.

A simultaneous broadband spectral analysis of SXT and LAXPC 20 was performed. LAXPC 20 was chosen since the LAXPC 20 data has less background compared to the others and since the spectrum is systematic dominated, including the other counters does not provide any significant improvement in the statistics. A gain correction was applied to the SXT spectrum using the Xspec command gain fit where the slope was fixed at unity and the best fit offset obtained was around ~ 1.3 eV. A constant factor was included in the model to allow for cross calibration variation between SXT and LAXPC spectra. For LAXPC the constant faction was fixed at unity while for SXT this factor was allowed to vary. An overall systematic error of 3% was included in the spectral fitting. For SXT the energy range considered for the fitting was 0.7-7.0 keV, while for LAXPC it was 4-30 keV, since beyond 30 keV, the LAXPC spectrum was dominated by the background. We fitted the combined spectra with a model consisting of interstellar absorption, a disc

emission and a thermal Comptonized component represented by the XSPEC models *Tbabs* (Wilms *et al.*, 2000), *diskbb* (Mitsuda *et al.*, 1984) and *thcomp* (Zdziarski *et al.*, 2020). Note that since *thcomp* is a convolution model, the model format used in XSPEC was *Tbabs*thcomp*diskbb* and we used the `energies` command, such that the model spectrum was computed for a wider energy range of **0.1-100 keV**. The fitted spectra is shown in Fig. 3.2 and the best fit parameters with errors in the 90% confidence level are listed in Table 3.1.

While a detailed spectral evolution of the source with different models and using all the AstroSat observations will be presented elsewhere, here we point out that during this observation, the spectrum of Cyg X-2 was typical with a soft component represented by a disc with inner radius temperature ~ 1.5 keV and thermal Comptonization from a corona with temperature ~ 3.5 keV having an optical depth of ~ 2.3 .

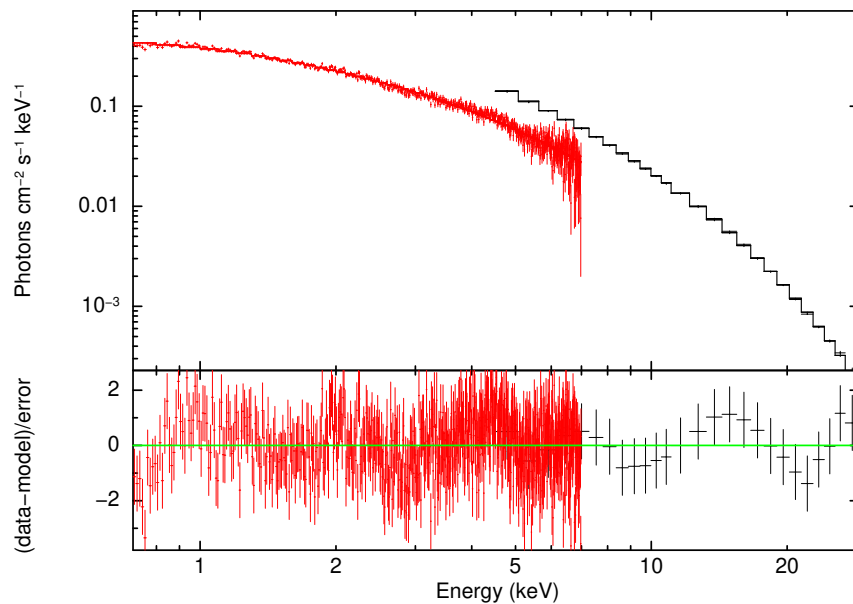


Figure 3.2: Spectra of LAXPC and SXT fitted with a model consisting of Comptonizing corona and disk emission with interstellar absorption with best fit parameters listed in Table 3.1. The black and red data points represent the LAXPC20 and SXT data respectively.

Table 3.1: X-ray Spectral Parameters of ObsID:9000000348 of Cyg X-2

Model Components	Parameters	Values
Tbabs	nH ($\times 10^{22} \text{cm}^{-2}$)	$0.06^{+0.01}_{-0.02}$
thcomp	Γ	$2.3^{+0.3}_{-0.5}$
	kT_e (keV)	$3.5^{+0.4}_{-0.4}$
	cov_{frac}	$0.7^{+0.3}_{-0.4}$
diskbb	kT_{in} (keV)	$1.5^{+0.1}_{-0.1}$
	N_{disk}	$70.2^{+22.8}_{-14.2}$
$\chi^2/\text{dof}=861.41/630$		

Note-(1) hydrogen column density in units of $\times 10^{22} \text{cm}^{-2}$, (2) Thomson optical depth, (3) corona electron temperature in keV, (4) covering fraction, (5) temperature at inner disk radius in keV and (6) diskbb normalisation.

3.2.2 Timing Analysis

We generated the power density spectrum (PDS) from the LAXPC data, using the using the command ‘laxpc_find_freqlag’ of the software LAXPCsoft Format A¹. The software created the full lightcurve in the 4.0-30 keV in 5 millisecond time-bin and divided it into 112 segments of 16384 time-bins. Power density spectrum for each segment was averaged and then rebinned in frequency. The resultant PDS in the frequency range 0.01-100 Hz is shown in Fig. 3.3 which reveals a prominent peak at ~ 42 Hz and broad band continuum noise. The high quality data shows complex broad band features, which required three Lorentzian functions (one for the ~ 42 Hz and two broad ones) and a power-law to fit the PDS even with a systematic error of 3%. The best fit parameters are listed in Table 3.2. The residuals suggest that perhaps the empirical broad Lorentzian functions are not adequate to describe the continuum noise or that the shapes of the features evolve in time and hence the time averaged PDS is not being well represented. Nevertheless, a clear strong QPO at ~ 42 Hz and broad continuum is clearly evident in the data. The PDS were extracted in the same manner for 4.0-6.0, 6.0-10.0, 10.0-30.0 keV bands and shown in Figure 3.4. It is evident from the figure that the variability increases with energy.

The LAXPC software task ‘laxpc_find_freqlag’ allows for the computation of the PDS for different energy bands, which is then used to estimate the Poisson noise subtracted and

¹<http://astrosat-ssc.iucaa.in/laxpcData>

background flux corrected, fractional r.m.s, f_{rms} for a frequency range Δf , as a function of energy. The code also generates using the cross-correlation function the energy dependent time-lag with respect to a reference energy band for a frequency range Δf . The top panel of Figure 3.5 shows the corresponding time-lags where the reference energy band is taken to be 10-15 keV one. The bottom panel shows the energy dependent f_{rms} for a $\Delta f \sim 3.9$ Hz centered at ~ 43 Hz, thus representing the QPO. Also plotted in the figure are the f_{rms} and time-lag corresponding to a $\Delta f \sim 39$ centered at ~ 11.7 Hz and hence representing the broad band continuum noise.

The fractional r.m.s increases with energy and has roughly the same shape for both the QPO and the continuum noise, indicating that most of the variability is in the higher energy thermal Comptonized spectral component. However, the energy dependent time-lag is qualitatively different for the QPO and the noise component. Negative time-lag at ~ 4 keV with respect to ~ 12 keV at the QPO frequency means that the high energy photons are delayed by about ~ 4.5 milli-seconds compared to the low energy ones. On the other hand, for the continuum noise the opposite is seen, such that the low energy photons are delayed by ~ 3.5 milli-seconds compared to the high energy ones. It should be noted that such a wide band energy dependence of the frms and time-lag has been possible due to the large effective area of the LAXPC instrument and the strength of the QPO during this observation.

Table 3.2: Power Density Spectral Parameters for a single observation of Cyg X-2

Model Components	Parameters	Values
Lorentz	Centroid (Hz)	$42.0^{+0.4}_{-0.4}$
	Width (Hz)	$8.7^{+1.1}_{-1.0}$
	rms (%)	$30.3^{+0.8}_{-0.7}$
	Centroid (Hz)	$0_0^{+0.1}$
	Width (Hz)	$16.1^{+0.4}_{-0.3}$
	rms (%)	$11.4^{+0.2}_{-0.2}$
	Centroid (milli-Hz)	110^{+1}_{-1}
	Width (Hz)	$0.013^{+0.01}_{-0.01}$
	rms (%)	$0.08^{+0.5}_{-0.5}$
Powerlaw	PhoIndex	$0.9^{+0.04}_{-0.04}$
	norm ($\times 10^{-4}$)	$1.1^{+0.08}_{-0.08}$

Note- PDS is fitted with three Lorentzian and a power law. All parameters are freed. $\chi^2=184.68$ dof=123

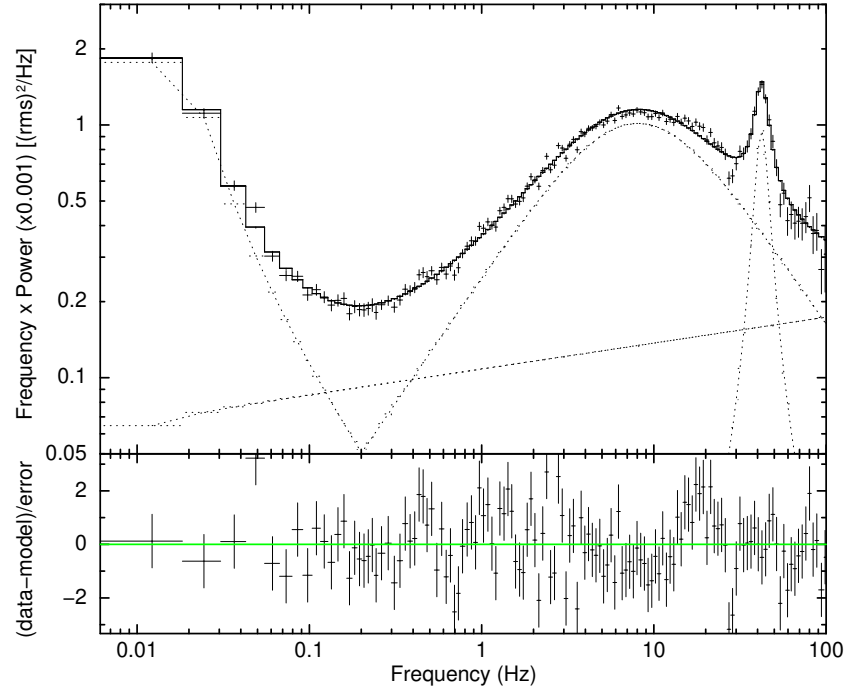


Figure 3.3: Power density spectrum of LAXPC from a single observation of Cyg X-2 in the 4.0-30.0 keV fitted with three Lorentzians and a power law.

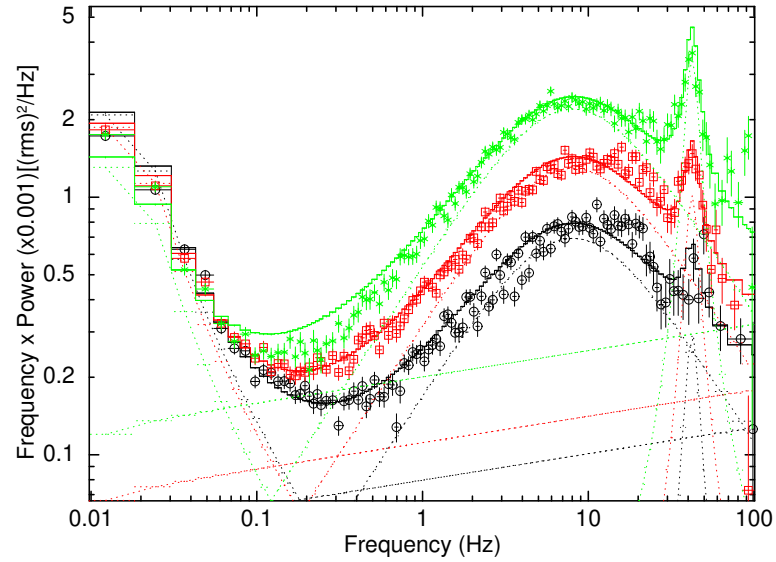


Figure 3.4: Power density spectra of LAXPC from a single observation of Cyg X-2 in the 4.0-6.0 keV (circle), 6.0-10.0 keV (box) and 10.0-30.0 keV (star) all fitted with three Lorentzians and a single powerlaw.

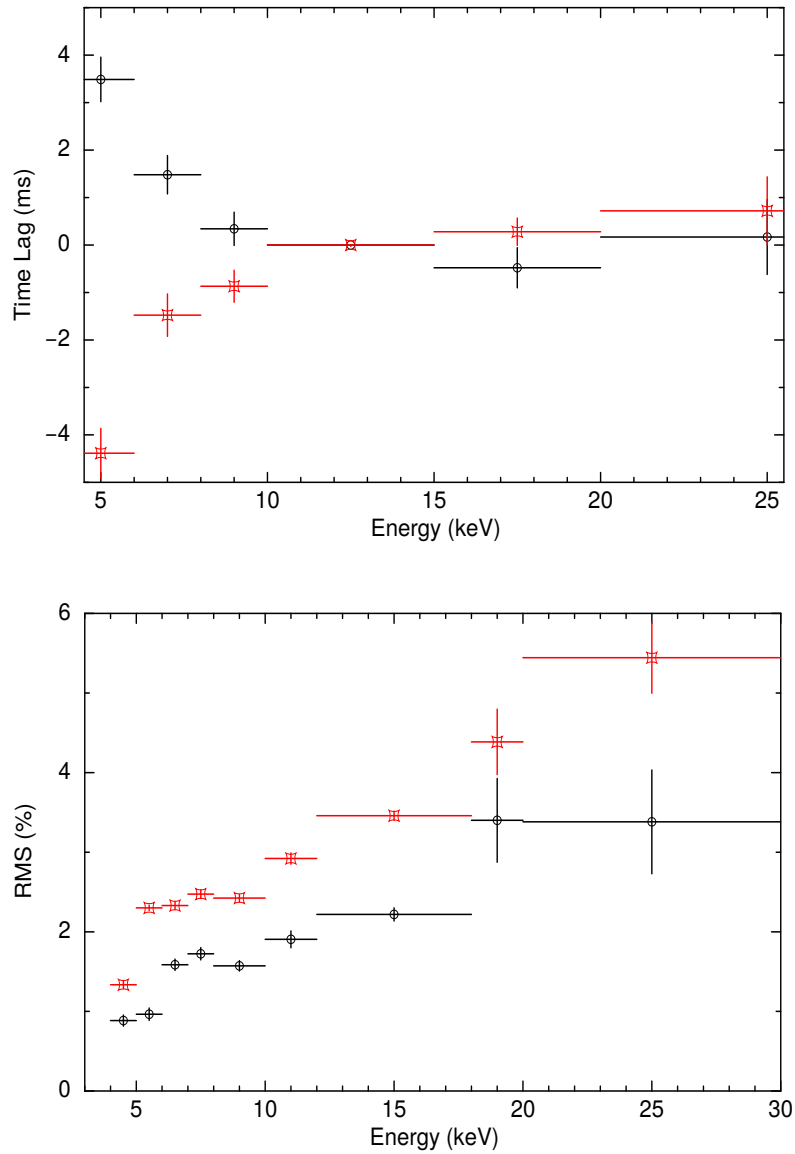


Figure 3.5: Time lag (top) and fractional r.m.s (bottom) and as a function of photon energy. For time-lag vs energy (top) the black denotes the ~ 10 Hz while red denotes the ~ 42 Hz. The black denotes the ~ 42 Hz while red denotes the ~ 10 Hz QPOs for the r.m.s vs energy (bottom).

3.3 Results and Discussion

In thermal Comptonization, photons at different energies have scattered a different number of times inside the medium, which due to scattering time-scale can produce energy dependent time-lags. Indeed, this is the model invoked to explain the energy dependent r.m.s and time-lags observed for the kHz QPO in neutron star systems (Lee *et al.*, 2008; Kumar & Misra, 2014; Karpouzas *et al.*, 2020). The model predicts both hard and

soft lags (the latter being observed in the lower kHz QPO), depending on the fraction of Comptonized photons that impinge back into the seed photon sources. The magnitude of the time lag is of the order of the light travel time through the corona and is measured to be ~ 50 microseconds for the kHz QPO. The time-lags found in this work for the ~ 42 Hz QPO are in the order of ~ 5 milli-seconds and hence it is unlikely to be due to Compton scattering effects, unless the size of the corona for this observation is ~ 100 times larger than when a kHz QPO is observed.

Time-lags significantly longer than those due to light travel time effects, can be explained in a framework where both the seed photon source and the Comptonizing medium coherently vary with a time-lag between them. As a specific example, a model where the heating rate of the corona and the temperature of the seed photon vary coherently with a time delay between them, can predict and fit the observed energy dependent r.m.s and time-lag for broad band noise and QPO of black hole systems (Maqbool *et al.*, 2019; Garg *et al.*, 2020). An obvious and generic feature of such models is that one gets hard lags when the coronal variation is delayed compared to that of soft photon source and the opposite soft lags occur when the soft seed photon source variation occurs after the coronal one.

In this work, we find that while the broad band noise at ~ 10 Hz exhibits soft lags, the ~ 42 Hz QPO shows hard lags. The simplest explanation for this is to evoke causality and state that the broad band noise is generated in the corona and propagates to the soft photon source, while the QPO is generated in the soft photon source and then propagates to the corona.

If the soft photon source is taken to be an accretion disc surrounding the Comptonizing medium, it is interesting to note that while the broad band noise is produced in the tenuous corona, the narrow coherent QPO is produced in the disc, making it tempting to identify the QPO frequency with the inner disc radius. From the best fit value of the disk normalization (Table 3.2) $n \sim 70$, and using a distance, $D \sim 13.5$ kpc (Jonker & Nelemans, 2004), inclination angle, $i \sim 60^\circ$ and colour factor, $f \sim 1.7$

(Shimura & Takahara, 1995), the inner radius of the disc can be estimated to be $R_{in} \sim f^2(D/10kpc)\sqrt{70/\cos(i)} \sim 45kms$. For a neutron star mass of $1.4M_{\odot}$, the Keplerian frequency at that radius is $\sim 240Hz$. The radius at which the Keplerian frequency would be equal to the QPO frequency of $\sim 42Hz$ is $\sim 140kms$. Given the uncertainty in the spectral fitting, the spectral model used and the colour factor, it maybe possible that the QPO is associated with the Kelperian frequency of the inner disc radius. Alternatively it could be associated with one of the other lower frequencies characteristic of that radius. Nevertheless, the results of this work indicate that the QPO orginates in the soft photon source and thus maybe associated with some charatceristic time-scale of the inner disc radius.

The result of this work had been published as “AstroSat detection of a quasi-periodic oscillation at ~ 42 Hz in Cygnus X-2,” in the Monthly Notices of the Royal Astronomical Society: Letters, Volume 512, Issue 1, May 2022, Pages L11-L15.

Chapter 4

Spectral behaviour of Cygnus X-2 along the Z-track

We report on the analysis of a Z-type neutron star low-mass X-ray binary source, Cygnus X-2 using five *AstroSat* observations taken in 2016 and 2019 respectively. The hardness intensity diagrams showed that the source went through all the branches of the Z-track i.e. the horizontal branch (HB), the normal branch (NB) and the flaring branch (FB) in the different observations undertaken here. Nigteen spectra were selected around different positions of the source in the HID for all the five observations. These spectra were fitted to a model consisting of interstellar absorption, a simple gaussian line at ~ 6.4 keV, a thermal Comptonized component and a disc emission or a mutli-blackbody component. In section 4.2 we will discuss the data reduction methodology of LAXPC and SXT, in section 4.2.1 we will discuss the spectral analysis. Under section 4.3 we have the results and discussion. Conclusions are placed under section 4.4.

4.1 Z-type sources of Neutron Star Low-mass X-ray Binary

The neutron star low-mass X-ray binary (NS LMXB) can be sub-divided into Z-type and Atoll-type sources based on X-ray spectral and fast timing behaviour (Hasinger & van der Klis, 1989). The Z sources trace out a Z-shape in the hardness-intensity or the X-ray color-color diagram. The branches of the Z-type sources are: horizontal branch (HB), normal branch (NB), and flaring branch (FB), from top to bottom. In the Z-track, the hard apex is the transition between the HB and the NB, and the soft apex is the transition between the NB and the FB. The variation of the mass transfer rate to the compact object (\dot{M}) is thought to produce the tracks (e.g. Hasinger & van der Klis 1989; Lamb, 1991). The hardness-intensity patterns of the Z-track sources are distinct, but there is no orbital related behaviour indicating a lower inclination, and the hardness-intensity patterns of the Atoll sources are quite different. A more fundamental classification would be based on luminosity, with Z-track sources having luminosities greater than $\sim 10^{38}$ erg

s^{-1} and Atoll sources having luminosities between $\sim 10^{36} \text{ erg } s^{-1}$ and $\sim 10^{38} \text{ erg } s^{-1}$, though not all lower luminosity LMXB have been identified as Atoll sources based on their hardness-intensity patterns. These patterns are also unknown, as is the relationship between the Z-track and Atoll classes, therefore understanding Z-track and Atoll sources remains a major challenge.

The Z sources are the brightest group of the Low Mass X-ray Binary source which contains a neutron star. The Z sources are classified into two groups (Kuulkers *et al.*, 1997; Hasinger & van der Klis, 1989), the Cyg-like sources- Cyg X-2, GX 5-1, GX 340+0 where the HB, NB, and FB are seen but with weak flaring and the Sco-like sources- Sco X-1, GX 349+2, GX 17+2 where flaring is strong and frequent but with a short or weak HB. Of all the Z sources, Cyg X-2 shows the most pronounced motion of the Z pattern in the HID. Using the Einstein MPC data, (Vrtilek *et al.*, 1986) witnessed one of the first observations of Z pattern motion in the HID. Not only do they observe a two factor increase in the intensity of various epochs, but they also observe an increase of an intensity on time scales less than a day. The behaviour of the Cyg X-2 Z track was not known at that time and thus the variations were interpreted as due to orbital effects. Now we know that the intensity variations are due to non-periodic motion of the source in the Z track and are also likely influenced with changes in M . In the study carried out by , Vrtilek *et al.*, 1986, the branches were found to shift wrt each other, this makes it the first indication that Cyg X-2 shows motion of the Z track in the HID. Previously, from the study carried out by (Chhange *et al.*, 2022), a QPO at $\sim 42\text{Hz}$ was detected where the source was in the horizontal branch of the Z-track.

Timing investigations, spectral studies, and theoretical studies are all possible approaches to understanding the Z-track sources. Timing studies have been conducted extensively to explore the QPOs detected in the Z-track and other sources (e.g. van der Klis *et al.*, 1987).

The source Cyg X-2 is classified as a Z-type source because of its behavior and pattern when studied on an X-ray color-color diagram and hardness-intensity diagram (HID)

(Hasinger & van der Klis, 1989; Hasinger, 1990; van der Klis, 2000). The LAXPC (Yadav *et al.*, 2016b; Agrawal *et al.*, 2017) instrument onboard the space observatory AstroSat (Agrawal, 2006; Singh *et al.*, 2014) has the advantage over RXTE by having a larger effective area at energies $\gtrsim 30$ keV. The SXT instrument (Singh *et al.*, 2016; Singh *et al.*, 2017) onboard provides simultaneous spectral coverage which has allowed for extensive spectro-timing studies of X-ray binaries (Leahy & Chen, 2019; Roy *et al.*, 2020).

4.2 Observations and Data Reduction

A detailed study of the spectral evolution of Cyg X-2 using all the available AstroSat data is presented here. We have taken five observations (Obs IDs: 9000000348, 9000002130, 9000002982, 9000003064, 9000003206) undertaken from February 28th 2016 to March 1st 2019. Spectra were fitted using XSPEC package, version 12.10.1 (Arnaud, 1996).

As already mentioned in Chapter 3, analysis of both LAXPC and SXT were done using the LAXPCSoft software and XSELECT respectively. To create the merged event files from the clean event files, we have used the SXT event merger tool. Spectra were fitted using XSPEC 12.10.1.

4.2.1 Spectral Analysis

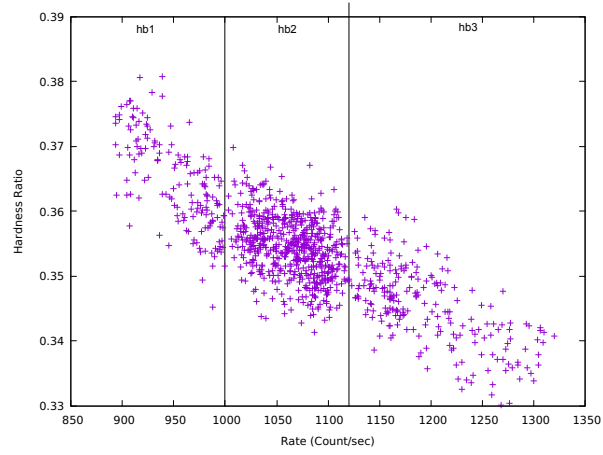
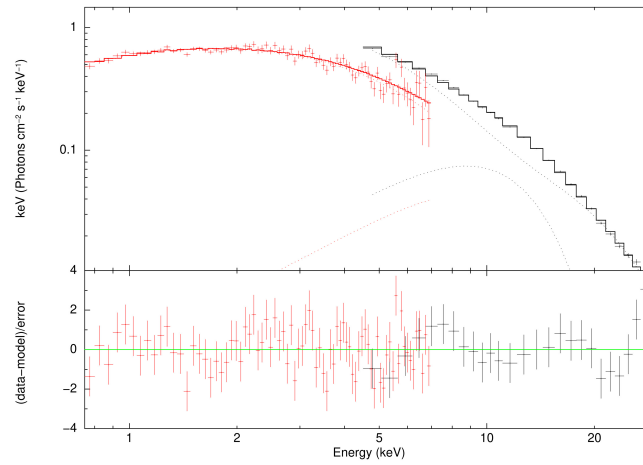
We have first examined the hardness intensity diagram (HID) of all the branches of each observation constructed using LAXPC lightcurves binned in 1.0 sec and in the energy ranges 3-8 keV (soft) and 8-20 keV (hard). The Hardness is defined as the ratio of the hard to soft bands. It can be seen from the analysis carried out that the source moves along the full Z-track during the observations in study and this consists of the Horizontal

Branch (HB), Normal Branch (NB) and the Flaring Branch (FB), the softapex as well as the hardapex were also observed. In order to investigate the spectral evolution along the Z-track, a total of 19 spectra were produced.

Here, a broad-band spectral analysis of *SXT* and LAXPC 20 were performed simultaneously for all the spectra of each observation. LAXPC 20 was chosen since the LAXPC 20 data has less background compared to the others and since the spectrum is systematic dominated, including the other counters does not provide any significant improvement in the statistics. A gain correction was applied to the *SXT* spectrum using the XSPEC command GAIN FIT where the slope was fixed at unity. A constant factor was included in all the models to allow for cross-calibration variation between *SXT* and LAXPC spectra. We have also included a fixed Gaussian line at 6.4 keV. An overall systematic error of 3% was included in the spectral fitting. For *SXT* the energy ranges considered for the fitting was 0.7-7.0 keV, while for LAXPC it was 4-30 keV.

Previously, the continuum spectra of Cyg X-2 was fitted by two-component models, the so-called Western model (White *et al.*, 1986) which consists of a blackbody component, originating close to the NS and a power law with high energy cut off (e.g. Hasinger, 1990 using Ginga data; Smale *et al.*, 1993 using BBXRT data) and the Eastern model (Mitsuda *et al.*, 1984) which consists of a multi-temperature blackbody from accretion disk and Comptonizes blackbody from the NS (e.g. Hasinger, 1990; Hoshi & Mitsuda, 1991 using Ginga data).

Here we have fitted the combined spectra of the various branches of all the observations with a model consisting of interstellar absorption, a simple gaussian line, a thermal Comptonized component and a disc emission or a multi-blackbody component represented by the XSPEC models *Tbabs* (Wilms *et al.*, 2000), *gaussian*, *thcomp* (Zdziarski *et al.*, 2020) and *diskbb* (Mitsuda *et al.*, 1984). Since *thcomp* is a convolution model, the model format used in XSPEC was *Tbabs(gaussian+thcomp*diskbb)* and we used the energies command, such that the model spectrum was computed for a wider energy range of 0.1-1000 keV.

Observation ID 9000000348**Figure 4.1:** HID of Observation 9000000348 with horizontal branches- HB1, HB2 and HB3**Figure 4.2:** LAXPC and SXT spectra of Obs 9000000348 in the region HB1 shown in Fig.4.1. Here the red lines denote SXT and the black line denotes LAXPC. The same color schematic is used for all figures of the LAXPC and SXT spectra.

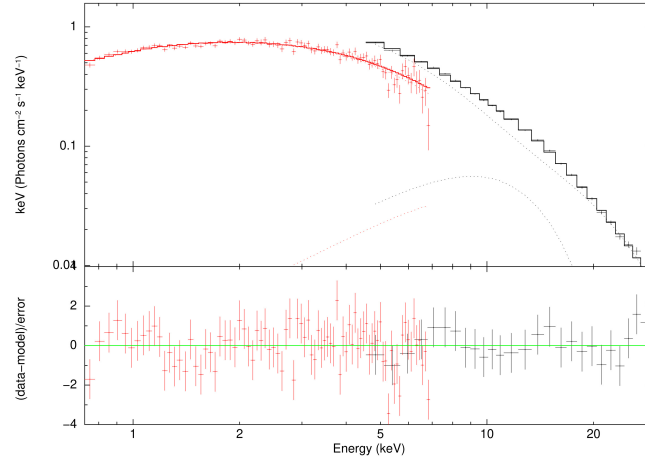


Figure 4.3: LAXPC and SXT spectra of Obs 9000000348 in the region HB2 shown in Fig.4.1

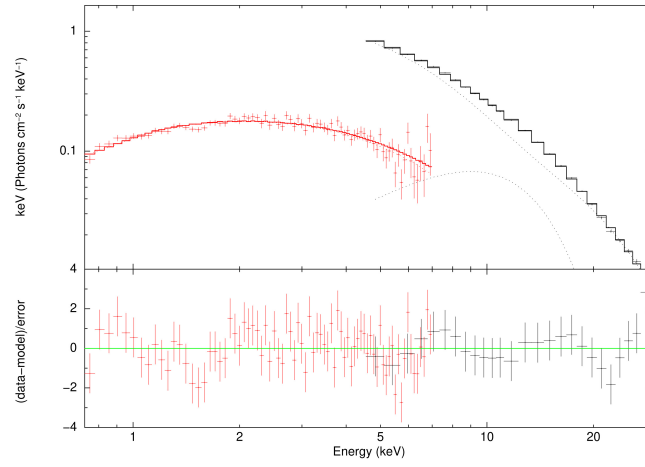


Figure 4.4: LAXPC and SXT spectra of Obs 9000000348 in the region HB3 shown in Fig.4.1

Table 4.1: X-ray Spectral Parameters of ObsID:9000000348 using models tbabs (Wilms *et al.*, 2000), gaussian, thcomp (Zdziarski *et al.*, 2020) and diskbb (Mitsuda *et al.*, 1984)

Model	Parameters	HB1	HB2	HB3
Tbabs	nH ($\times 10^{22} \text{cm}^{-2}$)	$0.05^{+0.03}_{-0.02}$	$0.06^{+0.02}_{-0.02}$	$0.1^{+0.03}_{-0.03}$
Gaussian	σ (keV)	$4.5^{+0.3}_{-0.2}$	$4.9^{+0.4}_{-0.4}$	$4.8^{+0.3}_{-0.3}$
	norm	$0.1^{+0.02}_{-0.02}$	$0.09^{+0.02}_{-0.03}$	$0.10^{+0.02}_{-0.02}$
thcomp	Γ_{τ}	$1.00^{+0.2}_{-1.00}$	$1.00^{+0.4}_{-1.00}$	$1.00^{+0.2}_{-1.00}$
	kT_e (keV)	3.50^f	3.50^f	3.50^f
	cov_{frac} (keV)	$0.02^{+0.02}_{-0.001}$	$0.02^{+0.05}_{-0.002}$	$0.02^{+0.03}_{-0.001}$
Diskbb	kT_{in} (keV)	$1.6^{+0.1}_{-0.1}$	$1.8^{+0.1}_{-0.1}$	$1.8^{+0.1}_{-0.1}$
	norm	$66.6^{+13.00}_{-11.00}$	$51.1^{+9.00}_{-8.00}$	$57.6^{+14.00}_{-10.00}$
cflux	thcomp	$0.1^{+0.05}_{-0.04}$	$0.1^{+0.04}_{-0.04}$	$0.1^{+0.04}_{-0.04}$
cflux	diskbb	$1.0^{+0.04}_{-0.04}$	$1.2^{+0.04}_{-0.04}$	$1.2^{+0.05}_{-0.04}$
cflux	gauss	$0.1^{+0.04}_{-0.03}$	$0.1^{+0.04}_{-0.04}$	$0.1^{+0.01}_{-0.02}$
cflux	Total	$1.5^{+0.06}_{-0.05}$	$1.3^{+0.04}_{-0.04}$	$1.5^{+0.06}_{-0.05}$
	R_{in}	12.00	10.00	11.00
	$\chi^2/\text{dof} =$	113.9/96	101.00/102	102.1/95

Note: All flux are of the order of $10^{-8} \text{ erg/cm}^2/\text{sec}$ for all tables of spectral parameters

Observation ID 9000003206

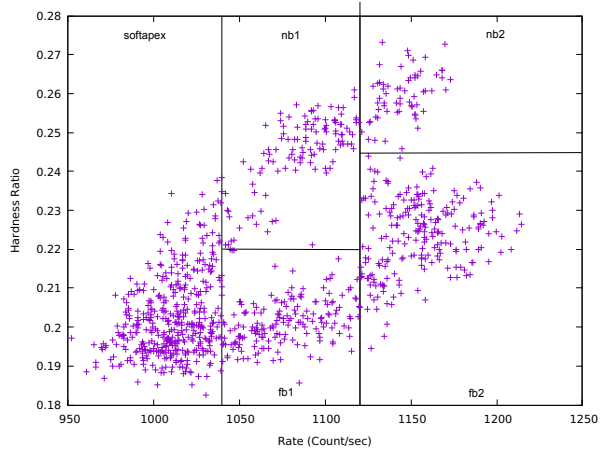


Figure 4.5: HID of Observation 9000003206 with different branches. From the bottom right, we have the flaring branches denoted by, FB1 and FB2. Then we have the softapex in the middle section followed by the normal branches, NB1 and NB2 on the upper right.

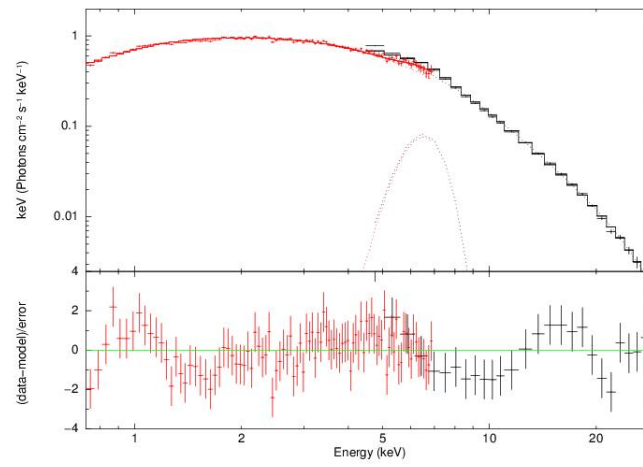


Figure 4.6: Spectra of LAXPC and SXT for Obs 9000003206 in the region FB1 shown in Fig.4.5

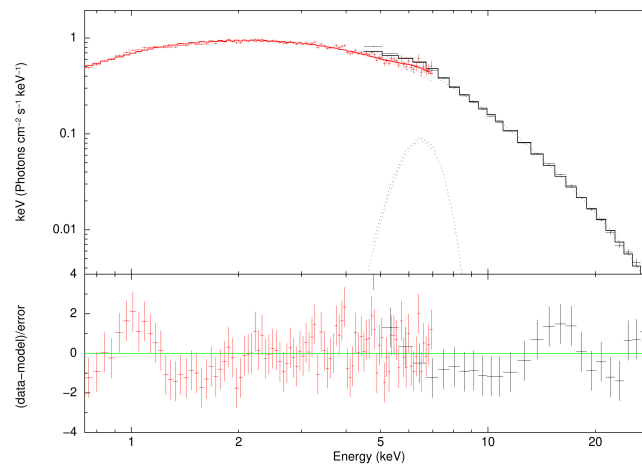


Figure 4.7: Spectra of LAXPC and SXT for Obs 9000003206 in the region FB2 shown in Fig.4.5

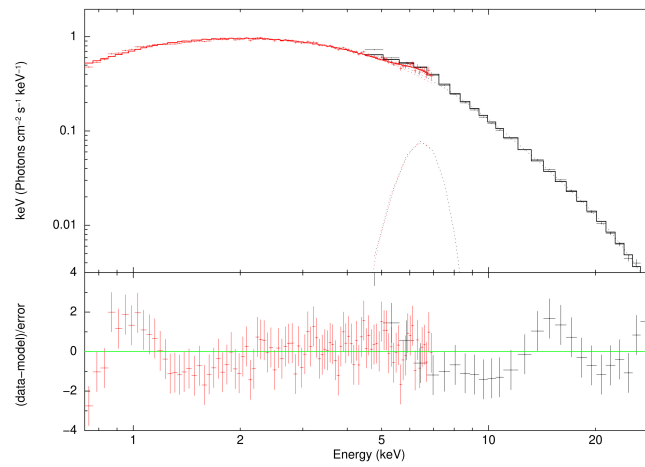


Figure 4.8: Spectra of LAXPC and SXT for Obs 9000003206 in the region Softapex shown in Fig.4.5

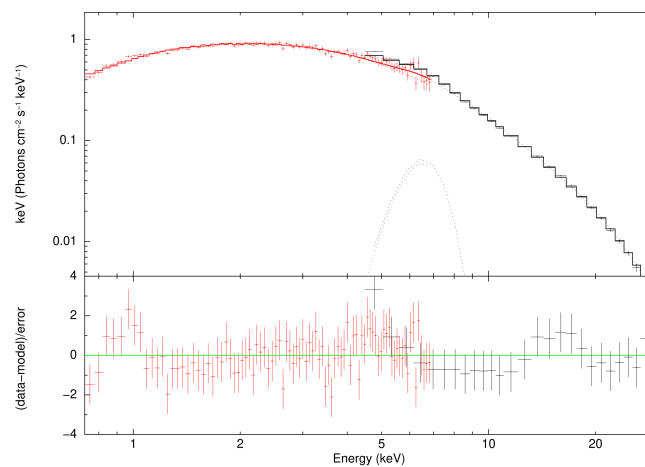


Figure 4.9: Spectra of LAXPC and SXT for Obs 9000003206 in the region NB1 shown in Fig.4.5

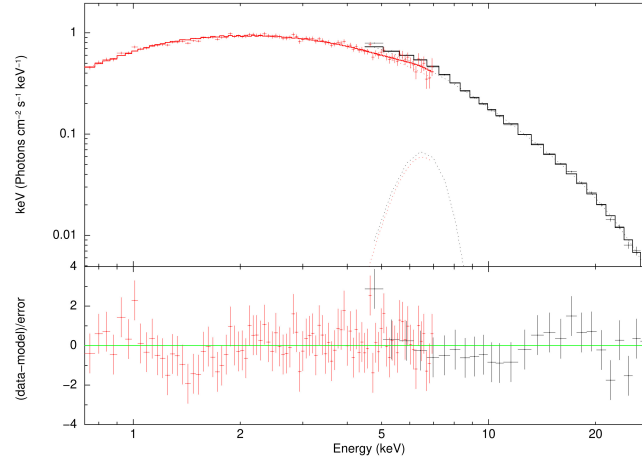


Figure 4.10: Spectra of LAXPC and SXT for Obs 9000003206 in the region NB2 shown in Fig.4.5

Table 4.2: X-ray Spectral Parameters of ObsID:9000003206 using models tbabs (Wilms *et al.*, 2000), gaussian, thcomp (Zdziarski *et al.*, 2020) and diskbb (Mitsuda *et al.*, 1984)

Model	Parameters	NB2	NB1	Softapex	FB1	FB2
Tbabs	nH ($\times 10^{22} \text{cm}^{-2}$)	$0.2^{+0.02}_{-0.02}$	$0.2^{+0.02}_{-0.02}$	$0.1^{+0.01}_{-0.01}$	$0.1^{+0.01}_{-0.01}$	$0.1^{+0.01}_{-0.01}$
Gaussian	σ (keV)	$0.9^{+0.3}_{-0.3}$	$0.9^{+0.3}_{-0.3}$	$0.7^{+0.2}_{-0.2}$	$0.8^{+0.2}_{-0.2}$	$0.8^{+0.2}_{-0.2}$
	norm	$0.02^{+0.01}_{-0.01}$	$0.02^{+0.01}_{-0.01}$	$0.02^{+0.01}_{-0.01}$	$0.03^{+0.01}_{-0.01}$	$0.03^{+0.01}_{-0.01}$
thcomp	Γ_{τ}	$1.1^{+0.01}_{-0.01}$	$1.0^{+4.00}_{-1.0}$	$1.0^{+1.0}_{-1.0}$	$1.3^{+0.01}_{-0.01}$	$1.3^{+1.0}_{-1.3}$
	kT_e (keV)	$3.1^{+0.1}_{-0.1}$	$3.0^{+0.3}_{-0.6}$	$3.0^{+0.3}_{-0.1}$	$3.0^{+0.1}_{-0.1}$	$3.0^{+0.1}_{-0.2}$
	cov_{frac}	$0.04^{+0.01}_{-0.01}$	$0.02^{+0.1}_{-0.002}$	$0.02^{+0.1}_{-0.002}$	$0.04^{+0.005}_{-0.005}$	$0.04^{+0.2}_{-0.03}$
Diskbb	kT_{in}	$1.8^{+0.05}_{-0.05}$	$1.8^{+0.04}_{-0.04}$	$1.7^{+0.03}_{-0.06}$	$1.7^{+0.04}_{-0.04}$	$1.8^{+0.1}_{-0.1}$
	norm	$53.7^{+7.5}_{-6.5}$	$51.9^{+9.3}_{-5.5}$	$55.2^{+6.3}_{-4.2}$	$55.3^{+6.0}_{-5.0}$	$49.3^{+7.7}_{-6.1}$
cflux	thcomp	$0.1^{+0.03}_{-0.06}$	$0.1^{+0.03}_{-0.04}$	$0.1^{+0.02}_{-0.04}$	$0.1^{+0.02}_{-0.04}$	$0.1^{+0.04}_{-0.04}$
cflux	diskbb	$1.1^{+0.03}_{-0.07}$	$1.0^{+0.03}_{-0.06}$	$1.0^{+0.02}_{-0.04}$	$1.0^{+0.02}_{-0.04}$	$1.1^{+0.04}_{-0.05}$
cflux	gauss	$0.02^{+0.03}_{-0.02}$	$0.02^{+0.03}_{-0.03}$	$0.02^{+0.02}_{-0.02}$	$0.02^{+0.02}_{-0.02}$	$0.03^{+0.02}_{-0.02}$
cflux	Total	$1.2^{+0.03}_{-0.01}$	$1.2^{+0.03}_{-0.03}$	$1.1^{+0.02}_{-0.02}$	$1.1^{+0.03}_{-0.02}$	$1.2^{+0.02}_{-0.02}$
R_{in}		10.5	10.2	10.5	10.5	10.0
$\chi^2/\text{dof} =$		88.6/107	101.1/106	123.8/124	139.4/112	128.5/111

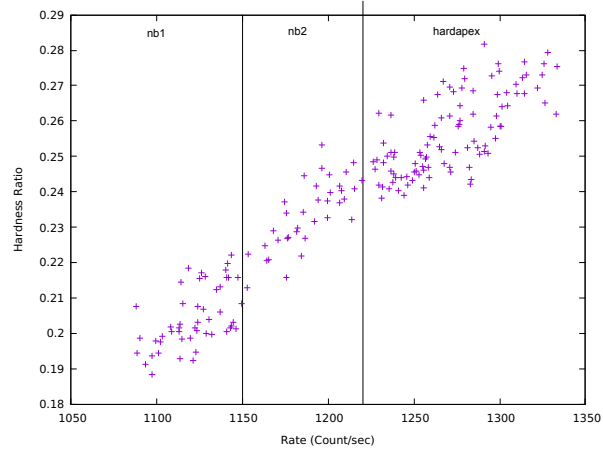
Observation ID 9000003064

Figure 4.11: HID of Observation 9000003064 with different branches. From the right we have the hardapex, followed by the normal branches NB2 and NB1 as we move towards the left.

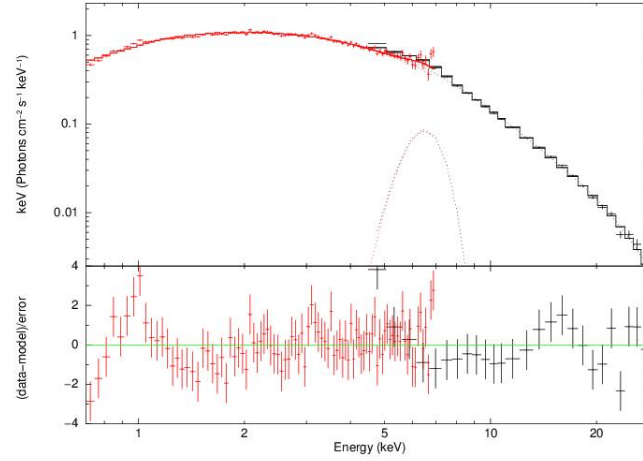


Figure 4.12: Spectra of LAXPC and SXT for Obs 9000003064 in the region NB1 shown in Fig.4.11

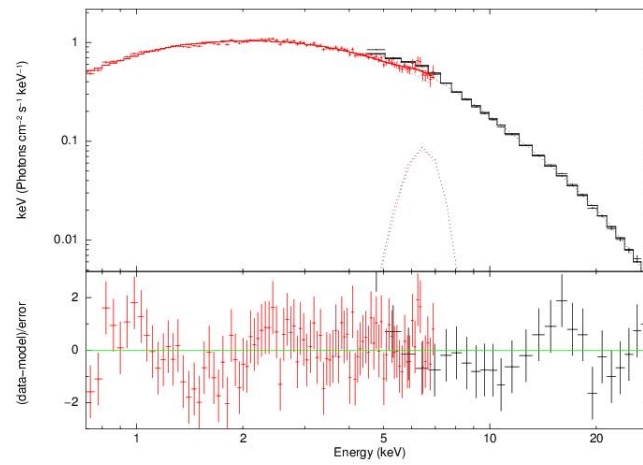


Figure 4.13: Spectra of LAXPC and SXT for Obs 9000003064 in the region NB2 shown in Fig.4.12

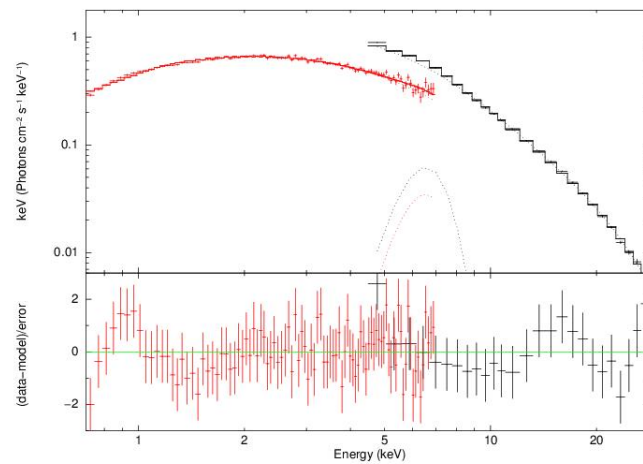


Figure 4.14: Spectra of LAXPC and SXT for Obs 9000003064 in the region Hardapex shown in Fig.4.11

Table 4.3: X-ray Spectral Parameters of ObsID:9000003064 using models tbabs (Wilms *et al.*, 2000), gaussian, thcomp (Zdziarski *et al.*, 2020) and diskbb (Mitsuda *et al.*, 1984)

Model	Parameters	Hardapex	NB2	NB1
Tbabs	nH ($\times 10^{22} \text{cm}^{-2}$)	$0.2^{+0.01}_{-0.01}$	$0.2^{+0.02}_{-0.02}$	$0.2^{+0.02}_{-0.02}$
Gaussian	σ (keV)	$0.9^{+0.3}_{-0.3}$	$0.6^{+0.3}_{-0.4}$	$0.7^{+0.2}_{-0.2}$
	norm	$0.02^{+0.01}_{-0.01}$	$0.02^{+0.01}_{-0.01}$	$0.02^{+0.01}_{-0.01}$
thcomp	Γ_{τ}	$1.2^{+1.0}_{-1.2}$	$1.0^{+1.0}_{-1.1}$	$1.0^{+4.0}_{-1.0}$
	kT_e (keV)	$3.2^{+0.6}_{-0.2}$	$3.1^{+0.4}_{-0.1}$	$3.3^{+0.3}_{-0.1}$
	cov_{frac} (keV)	$0.04^{+0.2}_{-0.03}$	$0.02^{+0.1}_{-0.01}$	$0.2^{+0.1}_{-0.002}$
Diskbb	kT_{in} (keV)	$1.8^{+0.1}_{-0.1}$	$1.7^{+0.05}_{-0.09}$	$1.6^{+0.04}_{-0.04}$
	norm	$58.3^{+12.0}_{-8.0}$	$59.8^{+11.0}_{-6.3}$	$71.8^{+10.0}_{-7.0}$
cflux	thcomp	$0.2^{+0.04}_{-0.05}$	$0.1^{+0.02}_{-0.05}$	$0.1^{+0.04}_{-0.04}$
cflux	diskbb	$1.2^{+0.1}_{-0.1}$	$1.2^{+0.03}_{-0.07}$	$1.1^{+0.03}_{-0.05}$
cflux	gauss	$0.02^{+0.03}_{-0.03}$	$0.02^{+0.01}_{-0.01}$	$0.03^{+0.04}_{-0.03}$
cflux	Total	$1.4^{+0.03}_{-0.03}$	$1.3^{+0.06}_{-0.05}$	$1.2^{+0.03}_{-0.03}$
R_{in}		11.0	11.0	12.0
$\chi^2/\text{dof} =$		88.9/111	105.0/109	147.9/110

Observation ID 9000002982

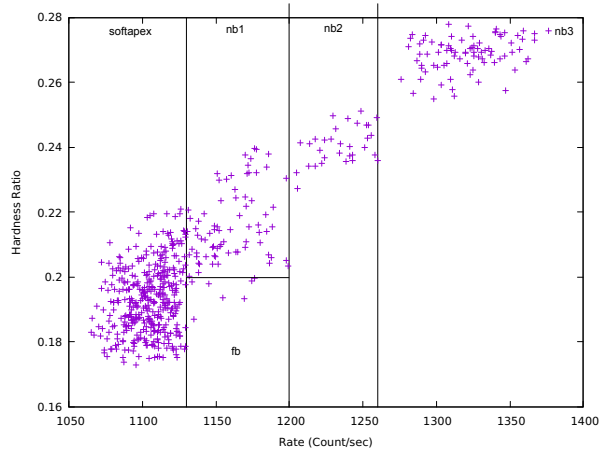


Figure 4.15: HID of Observation 9000002982 with different branches. Starting from the bottom we have a single flaring branch, FB, followed by the softapex. Moving upwards we can see the normal branches denoted by NB1, NB2 and NB3.

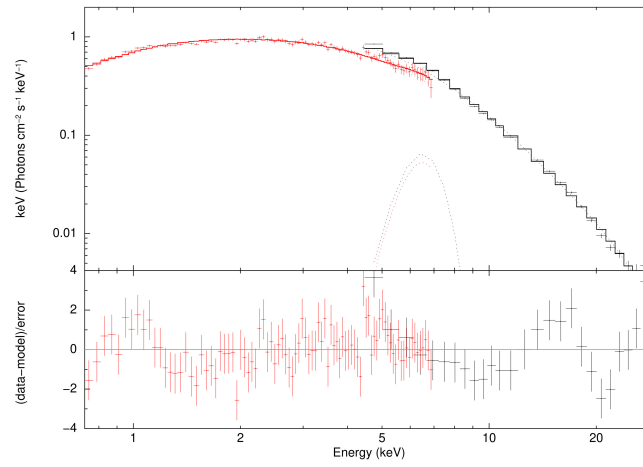


Figure 4.16: Spectra of LAXPC and SXT for Obs 9000002982 in the region FB shown in Fig.4.15

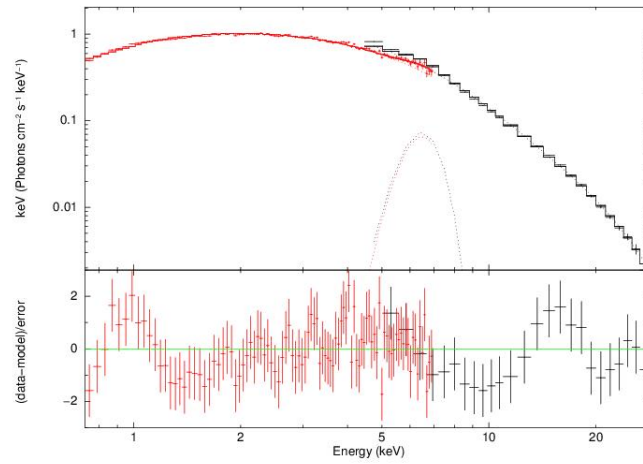


Figure 4.17: Spectra of LAXPC and SXT for Obs 9000002982 in the region Softapex shown in Fig.4.15

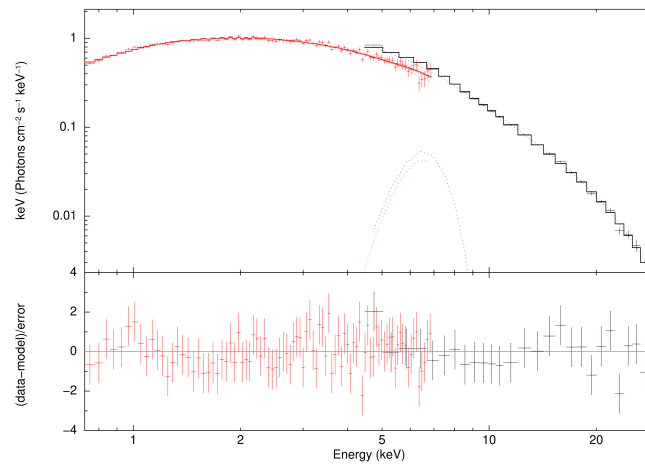


Figure 4.18: Spectra of LAXPC and SXT for Obs 9000002982 in the region NB1 shown in Fig.4.15

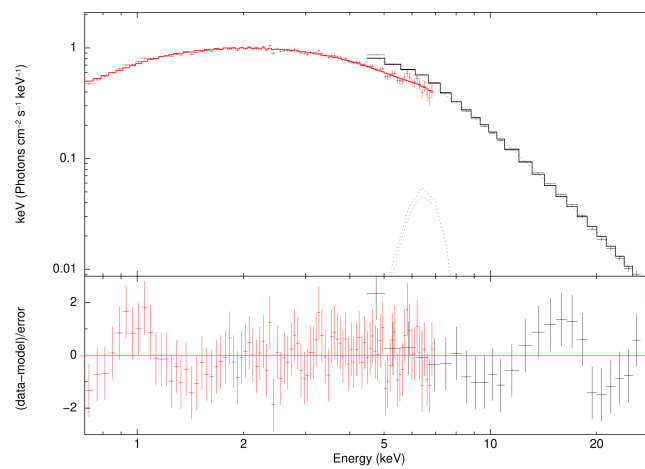


Figure 4.19: Spectra of LAXPC and SXT for Obs 9000002982 in the region NB2 shown in Fig.4.15

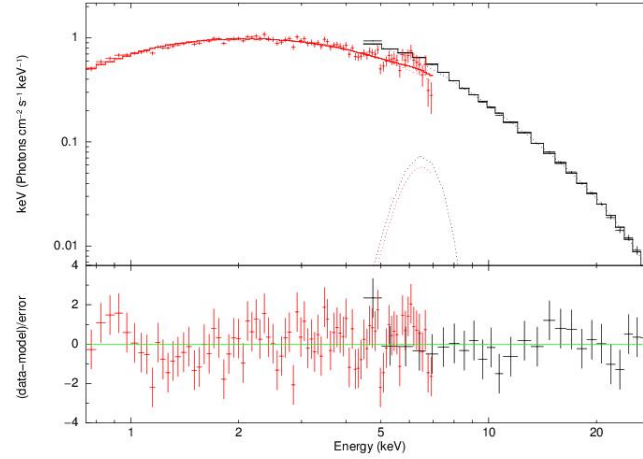


Figure 4.20: LAXPC and SXT spectra of Obs 9000002982 in the region NB3 shown in Fig.4.15

Table 4.4: X-ray Spectral Parameters of ObsID:9000002982 using models tbabs (Wilms *et al.*, 2000), gaussian, thcomp (Zdziarski *et al.*, 2020) and diskbb (Mitsuda *et al.*, 1984)

Model	Parameters	NB3	NB2	NB1	Softapex	FB
Tbabs	nH ($\times 10^{22} \text{cm}^{-2}$)	$0.1^{+0.02}_{-0.02}$	$0.1^{+0.02}_{-0.02}$	$0.1^{+0.02}_{-0.02}$	$0.2^{+0.01}_{-0.01}$	$0.1^{+0.02}_{-0.02}$
Gaussian	σ (keV)	$0.8^{+0.3}_{-0.3}$	$0.7^{+0.4}_{-0.3}$	$0.9^{+0.3}_{-0.4}$	$0.7^{+0.2}_{-0.2}$	$0.8^{+0.3}_{-0.4}$
	norm	$0.02^{+0.01}_{-0.01}$	$0.01^{+0.005}_{-0.01}$	$0.02^{+0.01}_{-0.01}$	$0.02^{+0.01}_{-0.01}$	$0.02^{+0.01}_{-0.01}$
thcomp	Γ_{τ}	$1.1^{+0.01}_{-0.01}$	$2.5^{+0.6}_{-0.6}$	$1.0^{+8.7}_{-1.0}$	$1.0^{+0.5}_{-1.0}$	$1.2^{+0.9}_{-1.2}$
	$kT_e(\text{keV})$	$3.1^{+0.1}_{-0.1}$	$4.8^{+3.0}_{-0.9}$	$2.8^{+0.1}_{-0.1}$	$2.8^{+0.5}_{-0.2}$	$3.0^{+0.5}_{-0.2}$
	cov_{frac}	$0.04^{+0.01}_{-0.01}$	$0.3^{+0.2}_{-0.1}$	$0.02^{+0.06}_{-0.002}$	$0.02^{+0.04}_{-0.002}$	$0.02^{+0.2}_{-0.01}$
Diskbb	kT_{in}	$1.8^{+0.05}_{-0.05}$	$1.6^{+0.02}_{-0.01}$	$1.6^{+0.04}_{-0.07}$	$1.6^{+0.03}_{-0.04}$	$1.7^{+0.05}_{-0.07}$
	norm	$61.8^{+7.5}_{-6.4}$	$75.8^{+12.2}_{-10.3}$	$81.9^{+12.8}_{-8.7}$	$70.0^{+8.0}_{-5.2}$	$64.4^{+10.1}_{-7.6}$
cflux	thcomp	$0.2^{+0.04}_{-0.07}$	$0.2^{+0.04}_{-0.04}$	$0.1^{+0.04}_{-0.05}$	$0.1^{+0.02}_{-0.04}$	$0.1^{+0.04}_{-0.04}$
cflux	diskbb	$1.3^{+0.05}_{-0.09}$	$1.4^{+0.03}_{-0.03}$	$1.2^{+0.04}_{-0.06}$	$1.1^{+0.02}_{-0.04}$	$1.2^{+0.04}_{-0.05}$
cflux	gauss	$0.02^{+0.04}_{-0.04}$	$0.01^{+0.04}_{-0.03}$	$0.02^{+0.04}_{-0.04}$	$0.02^{+0.03}_{-0.02}$	$0.02^{+0.03}_{-0.04}$
cflux	Total	$1.5^{+0.04}_{-0.04}$	$1.4^{+0.04}_{-0.03}$	$1.3^{+0.04}_{-0.03}$	$1.2^{+0.03}_{-0.02}$	$1.2^{+0.04}_{-0.03}$
R_{in}		11.1	12.3	12.8	11.8	11.3
$\chi^2/\text{dof} =$		102.8/101	87.2/111	78.1/106	121.7/114	145.4/107

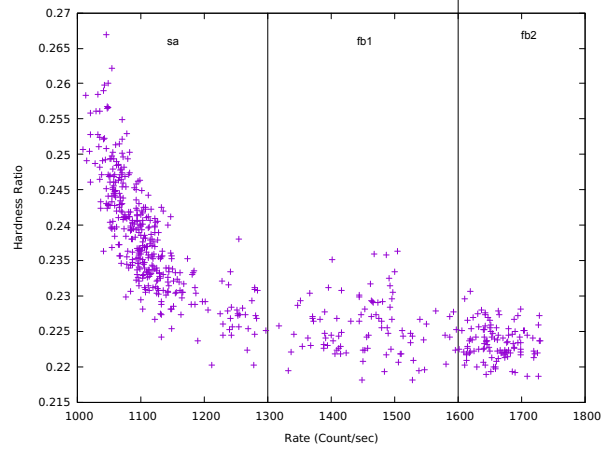
Observation ID 9000002130

Figure 4.21: HID of Observation 9000002130 with different branches. From the right we have the flaring branches FB2 and FB1 moving towards the softapex.

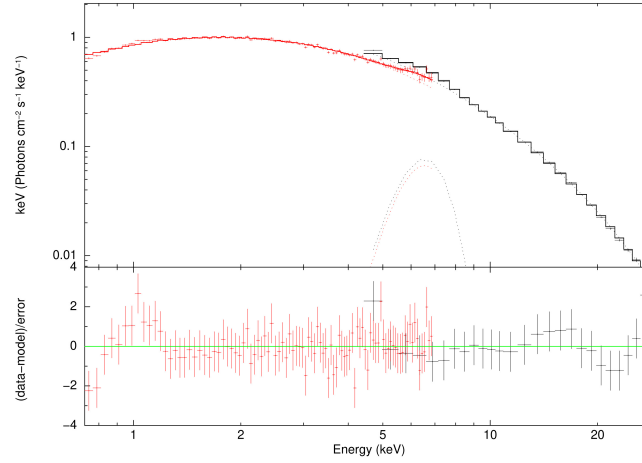


Figure 4.22: LAXPC and SXT spectra of Obs 9000002130 in the region NB1 shown in Fig.4.21

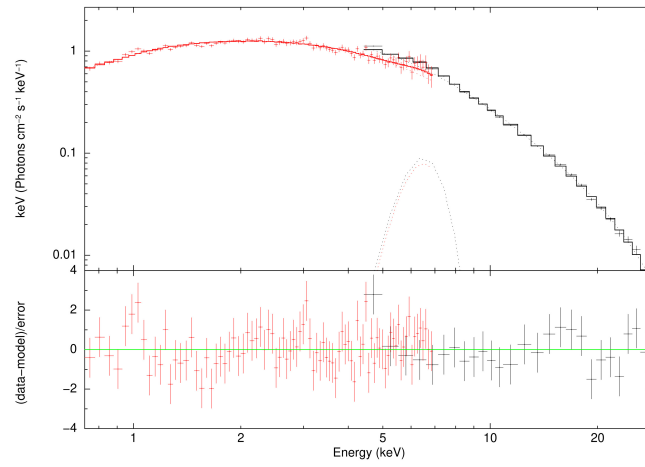


Figure 4.23: LAXPC and SXT spectra of Obs 9000002130 in the region NB2 shown in Fig.4.21

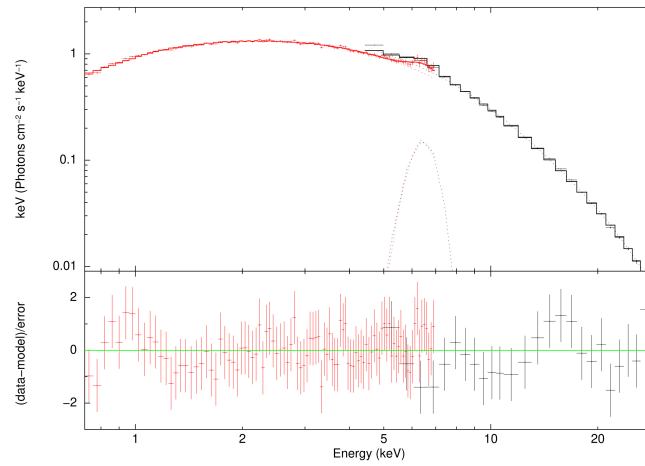


Figure 4.24: LAXPC and SXT spectra of Obs 9000002130 in the region NB3 shown in Fig.4.21

Table 4.5: X-ray Spectral Parameters of ObsID:9000002130 using models tbabs (Wilms *et al.*, 2000), gaussian, thcomp (Zdziarski *et al.*, 2020) and diskbb (Mitsuda *et al.*, 1984)

Model	Parameters	SA	FB1	FB2
Tbabs	nH ($\times 10^{22} \text{cm}^{-2}$)	$0.09^{+0.01}_{-0.01}$	$0.1^{+0.02}_{-0.02}$	$0.1^{+0.01}_{-0.01}$
Gaussian	σ (keV)	$0.9^{+0.2}_{-0.3}$	$0.8^{+0.4}_{-0.5}$	$0.6^{+0.3}_{-0.3}$
	norm	$0.03^{+0.01}_{-0.01}$	$0.03^{+0.02}_{-0.01}$	$0.04^{+0.01}_{-0.01}$
thcomp	Γ_{τ}	$2.8^{+0.1}_{-0.2}$	$1.3^{+0.8}_{-0.3}$	$1.6^{+0.9}_{-0.5}$
	kT_e (keV)	$4.5^{+0.4}_{-0.4}$	$3.1^{+0.5}_{-0.6}$	$3.4^{+0.7}_{-0.3}$
	cov_{frac} (keV)	$1.0^{+1.0}_{-0.2}$	$0.07^{+0.07}_{-0.04}$	$0.1^{+0.3}_{-0.1}$
Diskbb	kT_{in} (keV)	$1.3^{+0.1}_{-0.1}$	$1.8^{+0.1}_{-0.1}$	$1.9^{+0.1}_{-0.1}$
	norm	$156.2^{+28.9}_{-27.8}$	$69.8^{+18.0}_{-12.2}$	$56.1^{+12.0}_{-9.1}$
cflux	thcomp	$0.4^{+0.04}_{-0.03}$	$0.2^{+0.1}_{-0.1}$	$0.2^{+0.06}_{-0.05}$
cflux	diskbb	$0.8^{+0.05}_{-0.03}$	$1.5^{+0.1}_{-0.1}$	$1.5^{+0.1}_{-0.1}$
cflux	gauss	$0.03^{+0.02}_{-0.03}$	$0.03^{+0.04}_{-0.04}$	$0.04^{+0.04}_{-0.04}$
cflux	Total	$1.3^{+0.02}_{-0.03}$	$1.7^{+0.04}_{-0.04}$	$1.8^{+0.04}_{-0.04}$
R_{in}		17.7	11.8	10.6
$\chi^2/\text{dof} =$		86.5/113	97.6/104	79.6/114

4.3 Results and Discussion

In order to study the spectral behaviour corresponding to the position of the Z-track, we have created the spectra for all the different states in each of the observation.

We have in total nineteen spectra for all the different state of the source in the HID. All the nineteen spectra were fitted to a model consisting of interstellar absorption, a simple gaussian line at ~ 6.4 keV, a thermal Comptonized component and a disc emission or a multi-blackbody component.

In the first observation, 9000000348, the source was found in the horizontal branch. Here the soft component was interpreted as the emission from the inner accretion disc with inner temperature, kT_{in} varying between ~ 1.6 and ~ 1.8 keV, and the inner disc radius, R_{in} varying between ~ 11.5 and ~ 10.7 kms. In this observation, the electron temperature, kT_e was kept frozen at 3.50 keV and the optical depth $\tau \sim 1$. For the three branches of HB we obtained a $\chi^2/\text{d.o.f}$ of 113.9/96, 101.0/102 and 102.1/95 (HB1, HB2 and HB3 respectively) (Table 4.1).

In the second observation, 90000003206, the source was found in the flaring branch and

the normal branch as well as in the transitional state, softapex. Here the inner temperature, kT_{in} was found to be varying between ~ 1.7 and ~ 1.8 keV with the lowest value ~ 1.70 keV at the soft apex indicating that the inner disc temperature decreases as the source moves from the flaring branch to the normal branch. The inner disc radius R_{in} was varying between ~ 10.5 and ~ 9.9 kms. The electron temperature, $kT_e \sim 3$ keV and the optical depth τ was again ~ 1 . For the five branches of NB, SA and FB the best fit to the continuum was found using the model mentioned earlier (see results in Table 4.2). We obtained $\chi^2/\text{d.o.f}$ of 88.6/107, 101.1/106, 123.8/124, 139.4/112 and 128.5/111 (NB2, NB1, SA, FB1 and FB2 respectively).

In the third observation, 9000003064, the source was in the normal branch and in the transitional state hardapex. Here the inner temperature, kT_{in} was found to be varying between ~ 1.8 and ~ 1.6 keV with the lowest value ~ 1.64 keV at the normal branch indicating that the inner disc temperature increases as the source approaches the horizontal branch as it moves from the normal branch. The inner disc radius R_{in} was varying between ~ 11 and ~ 12 kms. The electron temperature, $kT_e \sim 3$ keV and the optical depth τ was again ~ 1 . For the three branches of HA and NB we obtained a $\chi^2/\text{d.o.f}$ of , 88.9/111, 105.0/109 and 147.9/110 (Table 4.3).

In the fourth observation, 9000002982, the source moves from the flaring branch to the transitional state softapex and then to the normal branch. The inner temperature, kT_{in} was found to be varying between ~ 1.8 and ~ 1.7 keV with the normal branch value increasing as it moves towards the upper branch . The inner disc radius R_{in} was ~ 11 kms. The electron temperature, $kT_e \sim 3$ keV and the optical depth τ was again ~ 1 . For the five branches of FB, SA and NB we obtained a $\chi^2/\text{d.o.f}$ of 102.8/101, 87.2/111, 78.1/106, 121.7 and 145.4/107 (NB3, NB2, NB1, SA and FB respectively) (Table 4.4).

In the fifth observation, 9000002130, the source moves from the flaring branch to the transitional state softapex. The inner temperature, kT_{in} was found to be varying between ~ 1.3 and ~ 1.9 keV with the flaring branch value decreasing as it moves towards the soft-apex and is lowest here . The inner disc radius R_{in} was varying between ~ 10.6 and ~ 17.7

kms. The electron temperature, kT_e varies quite a lot between ~ 3.4 keV and ~ 4.5 keV and the optical depth τ was also found to be varying between ~ 1.6 and ~ 2.8 . For the three branches of FB and SA we obtained a $\chi^2/\text{d.o.f}$ of 86.5/113, 97.6/104 and 79.6/114 (SA, FB1 and FB2 respectively) (Table 4.5).

4.4 Conclusions

Here we see that the source was in various part of the branch for different set of observations. Most of the branch follows that the soft component increases as we move from left to right along the branch. We see that in Table 4.1, the inner disc radius increases from the left to the right. The same is seen in the second observation where the inner disc radius increases gradually as we move from the NB to FB, and is lowest at softapex (Table 4.2). Also in the fifth observation, similar pattern is seen (Table 4.5). In the second observation, we see that the temperature is lowest at the softapex ~ 1.70 . Similarly in case of the fifth observation we see that the temperature is lowest at the softapex ~ 1.2 , this suggests that for both the second and fifth observation the mass accretion rate \dot{M} is low. Also at this point R_{in} is maximum at 10.5 km for the second observation and maximum at 17.7 km for the fifth observation, which is found to be consistent with the whole neutron star surface being emitting (Balucinska-Church, 2010).

So in our spectral deconvolution, for the horizontal branch of the first observation, the transition from the NB to FB in the second observation, transition from the soft apex to the FB of the fifth observation, they can be ascribed to a variation of the soft blackbody component, and this becomes harder as they move along from left to right along the branches. From here we interpret the soft blackbody component in the spectra of the Z sources as emission from inner accretion disc.

However, the inner disc is found to be decreasing in the case of the third and fourth observation (Table 4.3, Table 4.4). This can be explained by an occultation of the Comptonizing region probably caused by matter in an inner flared disk, or by an evolution from a spher-

ical to non-spherical geometry of the Comptonising cloud (T.DiSalvo, 2002).

The work done here is under communication.

Chapter 5

Summary and Conclusions

In this chapter we have summarised the conclusions of this thesis and have outlined the future prospects.

The hardness-intensity plot obtained using LAXPC data showed that the source was on the horizontal branch of the Z-track and the power density spectrum revealed the presence of a prominent Quasi-periodic Oscillation (QPO) at ~ 42 Hz with broad band continuum noise at lower frequencies. The large effective area of LAXPC at $\gtrsim 30$ keV, allowed for an unprecedented study of the energy dependence of the ~ 42 QPO and the broad noise continuum at ~ 10 Hz. The fractional r.m.s increases with energy and its shape is similar for both the QPO and the continuum noise suggesting a common radiative origin. However, while the QPO exhibits hard time lags, with the high energy photons lagging the low ones by a few milliseconds, the opposite behaviour is shown by the continuum noise, with the low energy photons lagging the high ones. The wide band photon spectrum from SXT and LAXPC in 0.7-30 keV band, is consistent with a soft component from a disc and a hard Comptonized component from a hot corona. While the energy dependence of the r.m.s shows that both the QPO and the continuum noise variability is dominated by the Comptonized component, the change in sign of the time-lag suggest that the dynamic origin of the QPO may be in the disk while the noise continuum may originate from the corona.

The time-lags found in this work for the ~ 42 Hz QPO are in the order of ~ 5 milliseconds and hence it is unlikely to be due to compton scattering effects, unless the size of the corona for this observation is ~ 100 times larger than when a kHz QPO is observed. In this work, we find that while the broad band noise at ~ 10 Hz exhibits soft lags, the ~ 42 Hz QPO shows hard lags. The simplest explanation for this is to evoke causality and state that the broad band noise is generated in the corona and propagates to the soft photon source, while the QPO is generated in the soft photon source and then propagates to the corona. From the best fit value of the disk normalization (Table 3.2) $n \sim 70$, and using a distance, $D \sim 13.5$ kpc (Jonker & Nelemans, 2004), inclination angle, $i \sim 60^\circ$

and colour factor, $f \sim 1.7$ (Shimura & Takahara, 1995), the inner radius of the disc can be estimated to be $R_{in} \sim f^2(D/10kpc)\sqrt{70/\cos(i)} \sim 45kms$. For a neutron star mass of $1.4M_{\odot}$, the Keplerian frequency at that radius is $\sim 240Hz$. The radius at which the Keplerian frequency would be equal to the QPO frequency of $\sim 42Hz$ is $\sim 140kms$. Given the uncertainty in the spectral fitting, the spectral model used and the colour factor, it may be possible that the QPO is associated with the Keplerian frequency of the inner disc radius. Alternatively it could be associated with one of the other lower frequencies characteristic of that radius. Nevertheless, the results of this work indicate that the QPO originates in the soft photon source and thus may be associated with some characteristic time-scale of the inner disc radius.

Also, using five *AstroSat* observations taken in 2016 and 2019 respectively, we studied the spectral changes across the various tracks of the source. The hardness intensity diagrams showed that the source went through all the branches of the Z-track i.e. the horizontal branch (HB), the normal branch (NB) and the flaring branch (FB) in the different observations undertaken here. Nineteen spectra were selected around different positions of the source in the HID for all the five observations. These spectra were fitted to a model consisting of interstellar absorption, a simple gaussian line at ~ 6.4 keV, a thermal Comptonized component and a disc emission or a multi-blackbody component.

In this work, we see that the source was in various part of the branch for different set of observations. Most of the branch follows that the soft component increases as we move from left to right along the branch. We see that in Table 4.1, the inner disc radius increases from the left to the right. The same is seen in the second observation where the inner disc radius increases gradually as we move from the NB to FB, and is lowest at softapex (Table 4.2). Also in the fifth observation, similar pattern is seen (Table 4.5). In the second observation, we see that the temperature is lowest at the softapex ~ 1.70 . Similarly in case of the fifth observation we see that the temperature is lowest at the softapex ~ 1.2 , this suggests that for both the second and fifth observation the mass accretion rate \dot{M} is low. Also at this point R_{in} is maximum at 10.5 km for the second observation and maximum at

17.7 km for the fifth observation, which is found to be consistent with the whole neutron star surface being emitting (Balucinska-Church, 2010).

So in our spectral deconvolution, for the horizontal branch of the first observation, the transition from the NB to FB in the second observation, transition from the soft apex to the FB of the fifth observation, they can be ascribed to a variation of the soft blackbody component, and this becomes harder as they move along from left to right along the branches. From here we interpret the soft blackbody component in the spectra of the Z sources as emission from inner accretion disc.

However, the inner disc is found to be decreasing in the case of the third and fourth observation (Table 4.3, Table 4.4). This can be explained by an occultation of the Comptonizing region probably caused by matter in an inner flared disk, or by an evolution from a spherical to non-spherical geometry of the Comptonising cloud (T.DiSalvo, 2002).

Future Prospect

From the lightcurve we have plotted, we observe various thermonuclear burst for the Cygnus X-2 source. It would be interesting to study the burst and interpret the data as well as compare the AstroSat's Cygnus X-2 results with that of other satellite of the same source.

In this work we were able to study only the spectral evolution of the Cygnus X-2 Z-track. it would be interesting to study the timing properties as well.

Bibliography

Agrawal, P. (2006). A broad spectral band Indian Astronomy satellite Astrosat, *Adv.Space Res.*, **38**, 2989-2994.

Agrawal, P. C. ; Yadav, J. S. ; Antia, H. M. ; Dedhia, Dhiraj ; Shah, P. ; Chauhan, Jai Verdhan ; Manchanda, R. K.; Chitnis, V. R. ; Gujar, V. M. ; Katoch, Tilak ; Kurhade, V. N. ; Madhwani, P. ; Manojkumar, T. K. ; Nikam, V. A. ; Pandya, A. S. ; Parmar, J. V. ; Pawar, D. M. ; Roy, Jayashree ; Paul, B. ; Pahari, Mayukh ; Misra, Ranjeev ; Ravichandran, M. H. ; Anilkumar, K. ; Joseph, C. C. ; Navalgund, K. H. ; Pandiyan, R. ; Sarma, K. S. ; Subbarao, K. (2017). Large Area X-Ray Proportional Counter (LAXPC) Instrument on AstroSat and Some Preliminary Results from its Performance in the Orbit, *J. Astrophys. Astron.*, **38**, 30.

Alpar, M. A. and Shaham, Ju. (1985). GX 5-1: a Possible Millisecond Period Neutron Star?, *IAUCs*, **4046**, 2.

Antia, H. M. ; Yadav, J. S. ; Agrawal, P. C. ; Chauhan, Jai Verdhan; Manchanda, R. K.; Chitnis, Varsha; Paul, Biswajit; Dedhia, Dhiraj; Shah, Parag; Gujar, V. M.; Katoch, Tilak; Kurhade, V. N.; Madhwani, Pankaj; Manojkumar, T. K.; Nikam, V. A.; Pandya, A. S.; Parmar, J. V.; Pawar, D. M.; Pahari, Mayukh; Misra, Ranjeev; Navalgund, K. H.; Pandiyan, R.; Sharma, K. S.; and Subbarao, K. (2017). Calibration of the Large Area X-Ray Proportional Counter (LAXPC) Instrument on board AstroSat, *ApJS*, **231**, 1.

- Antia, H. M.; Agrawal, P. C.; Dedhia, Dhiraj; Katoch, Tilak; Manchanda, R. K. ; Misra, Ranjeev; Mukerjee, Kallol; Pahari, Mayukh; Roy, Jayashree; Shah, P.; Yadav, J. S. (2021). Large Area X-ray Proportional Counter (LAXPC) in orbit performance: Calibration, background, analysis software, *J. Astrophys. Astron*, **42**, 32.
- Arnaud, H. (1996). XSPEC: The First Ten Years, *Astronomical Data Analysis Software and Systems V. Astron. Soc. Pac*, **101**, 17.
- Balucinska-Church, Monika and Gibiec, Andrzej and Jackson, NK and Church, Michael J. (2010). On the nature of the Cygnus X-2 like Z-track sources, *A&A*, **512**, A9.
- Belloni, T. and Psaltis, D. and van der Klis, M. (2002). A unified description of the timing features of accreting X-ray binaries, *ApJ*, **572**, 392.
- Bradt, H.V., Rothschild, R. E. and Swank, J. H. (1995). X-ray timing explorer mission, *Non-accelerator Particle Physics: Proceedings Of The International Conference*, 281.
- Byram, E. T., Chubb, T. A. and Friedman, H. (1996). Cosmic X-ray Sources, Galactic and Extragalactic. *Science*, **152**, 66-71.
- Casares, J., Charles, P. and Kuulkers, E. (1998). The Mass of the Neutron Star in Cygnus X-2 (V1341 Cygni) *ApJ*, **493**, 1.
- Chauhan, Jai Verdhan and Yadav, JS and Misra, Ranjeev and Agrawal, PC and Antia, HM and Pahari, Mayukh and Sridhar, Navin and Dedhia, Dhiraj and Katoch, Tilak and Madhwani, P and others. (2017). AstroSat/LAXPC Detection of Millisecond Phenomena in 4U 1728-34, *ApJ*, **841**, 41.
- Chhange, Vanzarmawii and Roy, Jayashree and Misra, Ranjeev and Zadeng, Lalthakimi. (2022). AstroSat detection of a quasi-periodic oscillation at 42 Hz in Cygnus X-2, *MNRAS*, **512**, L11-L15.

- Church, M. J., Gibiec, A., Balucinska-Church, M. and Jackson, N. K.(2012). Spectral investigations of the nature of the Scorpius X-1 like sources, *AAP*, **546**, A35.
- Cowley, A. P., Crampton, D. and Hutchings, J. B(1979). The Halo Population X-ray Source Cygnus X-2, *ApJ*, **231**, 539-550.
- Di Salvo, T. and Farinelli, R. and Burderi, L. and Frontera, F. and Kuulkers, E. and Masetti, N. and Robba, N. R. and Stella, L. and van der KApJSlis, M(2002). On the spectral evolution of Cygnus X–2 along its color-color diagram. *AAP*, **386**, 535-547.
- Elsner, R. F., Weisskopf, M. C., Darbro, W., Ramsey, B. D., Williams, A. C.(1986). Observations of Quasi-Periodic Oscillations GX 5-1 and Cygnus X-2 with the EIN-STEIN (HEAO-2) Observatory, *ApJ*, **308**, 655-660.
- Ford, E. C. and van der Klis, M.(1998). Strong Correlation between Noise Features at Low Frequency and the KilohertzQuasi-Periodic Oscillations in the X-Ray Binary 4U 1728–34, *ApJ*, **506**, L39.
- Forman W. and Jones C. and Cominsky L. and Julien P. and Murray S. and Peters G. and Tananbaum H., et al. The Fourth Uhuru Catalog of X-ray Sources(1978), *ApJS*, **38**. 357-412.
- Frank, J. and King, A. and Raine,D.(1992). Accretion power in astrophysics, **21**.
- Frontera, F. and Dal Fiume, D. and Malaguti, G. and Nicastro, L. and Orlandini, M. and Palazzi, E. and Pian, E. and Favata, F. and Santangelo, A.(1999). High energy properties of X-ray sources observed with BeppoSAX, *Nucl. Phys. B., Proceedings Supplements*, **69**, 286-293.
- Garg, A. and Misra, R. and Sen, S.(2020). Identifying the radiative components responsible for quasi-periodic oscillations of black hole systems, *MNRAS*, **499**, 2757-2765.

- Ghosh, P. and Lamb, F. K.(1992). Diagnostics of Disk-Magnetosphere Interaction in Neutron Star Binaries, *In: van den Heuvel E.P.J., Rappaport S.A. (eds) X-Ray Binaries and Recycled Pulsars. NATO ASI Series (Series C: Mathematical and Physical Sciences)*, **377**.
- Giacconi, R. and Gursky, H. and Paolini, F. R. and Rossi, B. B.(1962). Evidence for X-Rays From Sources Outside the Solar System, *PRL*, **9**, 439-443.
- Hasinger, G., Langmeier, A., Sztajno, M., Trumper, J., Lewin, W.H.G., White, N.E.(1986). Quasi-periodic oscillations in the X-ray flux of Cyg X-2, *Nat*, **319**, 468-471.
- Hasinger, G. and van der Klis, M.(1989). Two patterns of correlated X-ray timing and spectral behaviour in low-mass X-ray binaries, *A & A*, **225**, 79-96.
- Hasinger, G.(1990). X-Ray Diagnostics of Accretion Disks, *Rev. Mon. Astron.*, **3**, 60-73.
- Hoshi, R and Mitsuda, K. (1991). Possible Model Spectra for Bright Low-Mass X-ray Binaries, *Publ. Astron. Soc, Japan*, **43**, 485-499.
- Iben Jr, I.(1991). Single and Binary Star Evolution, *ApJS*, **76**, 55.
- Jonker, P. G. and Wijnands, R. and van der Klis, M. and Psaltis, D. and Kuulkers, E. and Lamb, F. K.(1998). Discovery of kilohertz quasi-periodic oscillations in the Z source GX 340+ 0, *ApJL*, **499**, L191.
- Jonker, P. G. and van der Klis, M. and Wijnands, R. and Homan, J. and van Paradijs, J. and Mendez, M. and Ford, E. C. and Kuulkers, E. and Lamb, F. K.(2000). The power spectral properties of the Z source GX 340+ 0, *ApJ*, **537**, 374.
- Jonker, P. G. and Nelemans, G.(2004). The distances to Galactic lowmass Xray binaries: consequences for black hole luminosities and kicks, *MNRAS*, **354**, 355-366.

- Kahn, S. M. and Grindlay, J. E.(1984). Evidence for weak X-ray burst emission from Cygnus X-2 and GX 17+2, *ApJ*, **281**, 826-829.
- Karpouzas, K., Mndez, M., Ribeiro, E. M., Altamirano, D., Blaes, O., Garca.(2020). The Comptonizing medium of the neutron star in 4U 1636 53 through its lower kilohertz quasi-periodic oscillations, *MNRAS*, **492**, 1399-1415.
- Kumar, N. and Misra, R.(2014). Energy dependent time delays of kHz oscillations due to thermal Comptonization, *MNRAS*, **445**, 2818-2824.
- Kuster, M.(2004). Combined Spectral and Temporal Analysis of a Her X-1 Turn-On. *Diss. Universitat Tübingen*
- Kuulkers, E and Van Der Klis, M. (1995). Detection of 26Hz quasi-periodic oscillations in the flaring branch of CygnusX-2, *A&A*, **303**, 801.
- Kuulkers, E. and Van Der Klis, M. and Vaughan, B. A.(1996). Secular variations in the Z source CygnusX-2, *AAP*, **311**, 197-210.
- Kuulkers, E., van der Klis, M., Oosterbroek, T., van Paradijs, J., Lewin, W. H. G.(1997). GX 17+2: X-ray spectral and timing behaviour of a bursting Z source, *MNRAS*, **287**, 495-514.
- Kuulkers, Erik and Wijnands, Rudy and Van Der Klis, Michiel.(1999). X-ray timing behaviour of Cygnus X-2 at low intensities, *MNRAS*. **308**, 485-492.
- Kuznetsov, S. I.(2002). Quasi-Periodic X-ray Oscillations in the Source Cygnus X-2, *Astron. Lett.*, **28**, 73-82.
- Lamb, F. K.(1989). Accretion by Magnetic Neutron Stars, In: *Ogelman H., van den Heuvel E.P.J. (eds) Timing Neutron Stars. NATO ASI Series (Series C: Mathematical and Physical Sciences)*, **262**.

- Lamb, F. K.(1991). Unified Model of X-ray Spectra and QPOs in Low Mass Neutron Star Binaries, *Neutron Stars: Theory and Observation, Dordrecht, Kluwer Academic Publishers*, **445**.
- Leahy, D. A. and Chen, Y. (2019). AstroSat SXT Observations of Her X-1, *ApJ*, **871**, 152.
- Lee, Hyong and Misra, R. and Taam, Ronald.(2008). A Compton Upscattering Model for Soft Lags in the Lower Kilohertz Quasi-periodic Oscillation in 4U 160852, *ApJ*, **549**, L229.
- Lewin, W. H. G. and van Paradijs, J. and van den Heuvel, E. P. J.(1995). X-ray binaries, *Camb. Astrophys. Ser.* **26**.
- Longair, M. S.(1994). High energy astrophysics. Vol.2: Stars, the galaxy and the interstellar medium, **2**.
- Maqbool, B., Mudambi, S. P., Misra, R. , Yadav, J. S. , Gudennavar, S. B. , Bubbly, S. G. , Rao, A., Jogadand, S., Patil, M. K., Bhattacharyya, S., Singh, K. P.(2019). A stochastic propagation model to the energy dependent rapid temporal behaviour of Cygnus X-1 as observed by AstroSat in the hard state, *MNRAS*, **486**, 2964-2975.
- Mendez, M. and van der Klis, M. and Wijnands, R. and Ford, E. C. and van Paradijs, J. and Vaughan, B. A.(1998). Kilohertz quasi-periodic oscillation peak separation is not constant in the Atoll source 4U 1608–52, *ApJL*, **505**, L23.
- Misra, Ranjeev and Yadav, JS and Chauhan, Jai Verdhhan and Agrawal, PC and Antia, HM and Pahari, Mayukh and Chitnis, VR and Dedhia, Dhiraj and Katoch, Tilak and Madhwani, P and others. (2017). AstroSat/LAXPC Observation of Cygnus X-1 in the Hard State, *ApJ*, **835**, 195.

- Mitsuda, K. , Inoue, H. , Koyama, K. , Makishima, K. , Matsuoka, M. , Ogawara, Y. , Shibazaki, N. , Suzuki, K. , Tanaka, Y. , Hirano, T.(1984). Energy spectra of low-mass binary X-ray sources observed from Tenma, *PASJ*, **36**, 741-759.
- Navalgund, K. H. ; Sarma, K. Suryanarayana; Gaurav, Piyush Kumar; Nagesh, G.; Annadurai, M. (2017). AstroSat Configuration and Realization, *J. Astrophys. Astron.*, **38**, 34.
- Norris, J. P. and Wood, K. S.(1986). Discovery of 5 Hz Quasi-periodic Oscillations in Cygnus X-2, *ApJ*, **312**, 732-738.
- Orosz, J. A. and Kuulkers, E.(1999). The optical light curves of Cygnus X-2 (V1341 Cyg) and the mass of its neutron star, *MNRAS*, **305**, 132-142.
- Peacock, A. and Andresen, R. D. and Manzo, G. and Taylor, B. G. and Villa, G. and Re, S. and Ives, J. C. and Kellock, S.(1981). The Gas Scintillation Proportional Counter on EXOSAT, *X-Ray Astronomy: Proceedings of the XV ESLAB Symposium held in Amsterdam, The Netherlands, 22–26 June 1981*, 525-534.
- Piraino, S. and Santangelo, A. and Kaaret, P.(2002). X-ray spectral and timing observations of Cygnus X-2, *ApJ*, **567**, 1091.
- Pringle, J. E. (1981). Accretion discs in astrophysics, *ARAA*, **19**, 137-162.
- Psaltis, D. and Lamb, F. K. and Miller, G. S.(1995). X-ray spectra of Z sources, *ApJ*, **454**, L137.
- Psaltis, D. and Belloni, T. and van der Klis, M. (1999). Correlations in quasi-periodic oscillation and noise frequencies among neutron star and black hole x-ray binaries, *ApJ*, **520**, 262.
- Psaltis, D. and Wijnands, R. and Homan, J. and Jonker, P. G. and van der Klis, M. and Miller, M. C. and Lamb, F. K. and Kuulkers, E. and van Paradijs, J. and Lewin, W.

- H. G. (1999). On the magnetospheric beat-frequency and Lense-Thirring interpretations of the horizontal-branch oscillation in the Z sources, *ApJ*, **520**, 763.
- Roy, J. ; Agrawal, P. C. ; Dedhia, D. K.; Manchanda, R. K.; Shah, P. B.; Chitnis, V. R.; Gujar, V. M.; Parmar, J. V.; Pawar, D. M.; Kurhade, V. B. (2016). Performance of large area x-ray proportional counters in a balloon experiment, *ApJ*, **42**, 249-270.
- Roy, Jayashree and Agrawal, PC and Iyer, NK and Bhattacharya, D and Yadav, JS and Antia, HM and Chauhan, JV and Choudhury, M and Dedhia, DK and Katoch, T and others. (2019). LAXPC/AstroSat Study of ~ 1 and ~ 2 mHz Quasi-periodic Oscillations in the Be/X-Ray Binary 4U 0115+ 63 during Its 2015 Outburst, *ApJ*, **872**, 33.
- Roy, Jayashree and Agrawal, Prahlad C and Singari, Baibhav and Misra, Ranjeev. (2020). AstroSat observation of the Be/X-ray binary Pulsar 3A 0726-260 (4U 0728-25), *Res. Astron. Astrophys*, **20**, 155.
- Shakura, N. I. and Sunyaev, R. A.(1973). Black holes in binary systems. Observational appearance, *AAP*, **24**, 337-355.
- Shimura, Toshiya and Takahara, Fumio. (1995). On the Spectral Hardening Factor of the X-Ray Emission from Accretion Disks in Black Hole Candidates, *ApJ*, **445**, 780.
- Singh, Kulinder Pal and Tandon, SN and Agrawal, PC and Antia, HM and Manchanda, RK and Yadav, JS and Seetha, S and Ramadevi, MC and Rao, AR and Bhattacharya, D and others. (2014). ASTROSAT Mission, *Proc. SPIE*, **9144**, 517-531.
- Singh, Kulinder Pal and Stewart, Gordon C and Chandra, Sunil and Mukerjee, Kallol and Kotak, Sanket and Beardmore, Andy P and Chitnis, Varsha and Dewangan, Gulab C and Bhattacharyya, Sudip and Mirza, Irfan and others. (2016). In-orbit performance of SXT aboard AstroSat, *SPIE*, **9905**, 389–398.

- Singh, KP and Stewart, GC and Westergaard, NJ and Bhattacharayya, S and Chandra, S and Chitnis, VR and Dewangan, GC and Kothare, AT and Mirza, IM and Mukerjee, K and others. (2017). Soft X-ray Focusing Telescope Aboard AstroSat: Design, Characteristics and Performance, *JApA*, **38**, 1-11.
- Smale, AP and Done, C and Mushotzky, RF and Weaver, KA and Serlemitsos, PJ and Marshall, FE and Petre, R and Jahoda, KM and Boldt, EA and Swank, JH and others (1993). Resolving the iron K line in Cygnus X-2- an observation with BBXRT, *ApJ*, **410**, 796-802.
- Smale, A. P. (1998). A Type I Burst with Radius Expansion Observed from Cygnus X-2 with the Rossi X-Ray Timing Explorer, *ApJ*, **498**, 141-145.
- Stella, L. and Vietri, M. (1997). Lense-Thirring precession and quasi-periodic oscillations in low-mass X-ray binaries, *ApJ*, **492**, L59.
- Strohmayer, T. E. and Zhang, W. and Swank, J. H. and Smale, A. and Titarchuk, L. and Day, C. and Lee, U. (1996). Millisecond X-ray variability from an accreting neutron star system, *ApJ*, **469**, L9.
- Tauris, T. M. and van den Heuvel, E. P. J. (2006). Formation and evolution of compact stellar X-ray sources, *Compact stellar X-ray sources*, **39**, 623-665.
- Di Salvo, T and Farinelli, R and Burderi, Luciano and Frontera, F and Kuulkers, E and Masetti, N and Robba, NR and Stella, L and van der Klis, M. (2002). On the Spectral Evolution of Cugnus X-2 along its color-color diagram, *A&A*, **386**, 535-547.
- Turner, M. J. L. and Smith, A. and Zimmermann, H. U. (1981). The medium energy instrument on EXOSAT, *X-Ray Astronomy: Proceedings of the XV ESLAB Symposium held in Amsterdam, The Netherlands, 22-26 June 1981*, 513-524.

- Van der Klis, M. and Jansen, F. and Van Paradijs, J. and Lewin, W. H. G. and Van den Heuvel, E. P. J. and Trumper, J.E. and Sztajno, M. (1985). Intensity-dependent quasi-periodic oscillations in the X-ray flux of GX5-1, *Nature*, **316**, 225-230.
- Van der Klis, M and Hasinger, G and Stella, L and Langmeier, A and Van Paradijs, J and Lewin, WHG. (1987). The complex cross-spectra of Cygnus X-2 and GX 5-1, *ApJ*, **319**, L13-L18.
- Van der Klis, M. (1989). Quasi-periodic oscillations and noise in low-mass X-ray binaries, *Annu. Rev. Astron. Astrophys.*, **27**, 517-553.
- Van der Klis, M. and Swank, J. H. and Zhang, W. and Jahoda, K. and Morgan, E. H. and Lewin, W. H. G. and Vaughan, B. and Van Paradijs, J. (1996). Discovery of submillisecond quasi-periodic oscillations in the X-ray flux of Scorpius X-1, *ApJ*, **469**, L1.
- Van der Klis, M. (1997). Kilohertz quasi-periodic oscillations in low-mass X-ray binaries, *Astronomical Time Series: Proceedings of The Florence and George Wise Observatory 25th Anniversary Symposium held in Tel-Aviv, Israel, 30 December 1996–1 January 1997*, 121-132.
- Van der Klis, M. and Wijnands, R. A. D and Horne, K. and Chen, W. (1997). Kilohertz quasi-periodic oscillation peak separation is not constant in Scorpius X-1, *ApJ*, **481**, L97.
- Van der Klis, M. (2000). Millisecond oscillations in X-ray binaries, *Annu. Rev. Astron. Astrophys.*, **38**, 717-760.
- Van Der Klis, M. (2006). Overview of QPOs in neutron-star low-mass X-ray binaries, *ASR*. **38**, 2675-2679.

- Vrtilek, SD and Kahn, SM and Grindlay, JE and Helfand, DJ and Seward, FD. (1986). Spectral Variability of Cygnus X-2- Structure in the circumsource material, *ApJ*, **307**, 698-710.
- White, NE and Peacock, A and Hasinger, G and Mason, KO and Manzo, G and Taylor, BG and Branduardi-Raymont, G. (1986). A study of the continuum and iron K line emission from low-mass X-ray binaries, *MNRAS*, **218**, 129-138.
- Wijnands, R. and Homan, J. and van der Klis, M. and Mendez, M. and Kuulkers, E. and van Paradijs, J. and Lewin, W. H. G. and Lamb, F. K. and Psaltis, D. and Vaughan, B. (1997). Discovery of kilohertz quasi-periodic oscillations in GX 17+ 2, *ApJ*, **490**, L157.
- Wijnands, R. A. D. ; van der Klis, M. ; Kuulkers, E. ; Asai, K. ; Hasinger, G. (1997). Ginga Observations of Cygnus X-2, *A&A*, **323**, 399.
- Wijnands, R. and Homan, J. and van der Klis, M. and Kuulkers, E. and van Paradijs, J. and Lewin, W. H. G. and Lamb, F. K. and Psaltis, D. and Vaughan, B. (1998). Discovery of kHz quasi-periodic oscillations in the Z source Cygnus X-2, *ApJL*, **493**, L87.
- Wijnands, R. and Mendez, M. and van der Klis, M. and Psaltis, D. and Kuulkers, E. and Lamb, F. K. (1998). Discovery of Kilohertz Quasi-periodic Oscillations in the Z Source GX 5–1, *ApJL*, **504**, L35.
- Wijnands, Rudy and Van Der Klis, Michiel. (2001). Normal-branch quasi-periodic oscillations during the high-intensity state of Cygnus X-2, *MNRAS*, **321**, 537-543.
- Wilms, J. and Allen, A. and McCray, R. (2000). On the Absorption of X-Rays in the Interstellar Medium, *ApJ*, **542**, 914-924.
- Yadav, JS and Misra, Ranjeev and Chauhan, Jai Verdhhan and Agrawal, PC and Antia, HM and Pahari, Mayukh and Dedhia, Dhiraj and Katoch, Tilak and Madhwani, P

and Manchanda, RK and others. (2016a). AstroSat/LAXPC reveals the high-energy variability of GRS 1915+ 105 in the χ class, *ApJ*, **833**, 27.

Yadav, JS and Agrawal, PC and Antia, HM and Chauhan, Jai Verdhhan and Dedhia, Dhiraj and Katoch, Tilak and Madhwani, P and Manchanda, RK and Misra, Ranjeev and Pahari, Mayukh and others. (2016b). Large Area X-ray Proportional Counter (LAXPC) instrument onboard ASTROSAT, *Proc. SPIE*, **9905**, 374-388.

Zeldovich, Y. B. and Guseynov, O. H. (1966). Collapsed Stars in Binaries, *ApJ*, **144**, 840.

Zdziarski, A. A, Szanecki, M., Poutanen, J., Gierlinski, M., Biernacki, P. (2020) Spectral and temporal properties of Compton scattering by mildly relativistic thermal electrons, *MNRAS*, **492**, 5234-5246.

LIST OF PUBLICATIONS AND ACTIVITIES

I. Journals:

1. **Chhangte, Vanzarmawii**; Misra, Ranjeev; Zadeng, Lalthakimi. (2020). Generation of Spectral and Timing Properties of Cygnus X-2 using AstroSat's Data. *JAFS*. 6(2), 70-78.
ISSN:2395-5554 (Print); 2395-5562 (Online). (Peer Reviewed)
2. **Chhangte, Vanzarmawii**; Roy, Jayashree; Misra, Ranjeev and Zadeng, Lalthakimi. (2022). AstroSat detection of a quasi-periodic oscillation at ~ 42 Hz in Cygnus X-2. *MNRAS*, 512(1), L11-L15. <https://doi.org/10.1093/mnrasl/slac014>.
3. **Chhangte, Vanzarmawii**; Roy, Jayashree; H Lalthantluanga; Misra, Ranjeev; Zadeng, Lalthakimi. (To be communicated). Spectral Evolution of Cygnus X-2 using AstroSat.

II. Conferences/ Workshops Attended

a. National:

1. Workshop on Gravitation and Gravitational Waves, 7th-13th October, 2018, Assam University, Silchar, Assam.
2. Trends in Modern Physics, 24th-25th February, 2020, Assam Don Bosco University, Assam. (**Poster presentation**)
3. Online Refresher Course on Astronomy and Astrophysics, 11th May-12th June, 2020, Inter-University Centre for Astronomy and Astrophysics, Pune.
4. Popular Talk on Astronomy, 25th July, 2020, Assam University, Silchar, Assam.
5. North-East Meet of Astronomers-VI, 10th-13th November, 2020, Indian Institute of Technology, Guwahati, Assam.
6. Advanced AstroSat Data Analysis Workshop, 21st-30th June, 2021, AstroSat Science Support Cell, Inter-University Centre for Astronomy and Astrophysics, Pune.

7. The Cosmos: Understanding Gravity and the Dynamics of the Universe, 30th June 2021, Mizoram Science Centre, Aizawl.
8. Research and Publication Ethics, 1st-7th October, 2021, UGC HRDC, Mizoram University.
9. 2nd China-India Workshop on High Energy Astrophysics, 6th-10th December, 2021, Inter-University Centre for Astronomy and Astrophysics, Pune.
10. AstroSat Calibration Meeting, 23rd-24th August, 2022, Inter-University Center for Astronomy and Astrophysics, Pune.
11. 3rd China-India Workshop on High Energy Astrophysics, 29th-30th August, 2022, Inter-University Centre for Astronomy and Astrophysics, Pune.
12. Seven years of Operation of AstroSat, 28th-29th September, 2022, ISRO, Bangalore. **(Oral Presentation)**
13. North-East Meet of Astronomers-VIII, 21st-23rd November, 2022, Manipur University, Manipur. **(Oral Presentation)**

b. International:

1. 44th COSPAR Scientific Assembly, 16th-24th July, 2022, Athens, Greece. **(Poster Presentation)**
2. History of Astronomy of the Mizo People, 18th-19th May, 2023, Department of Physics and Mizoram Science Centre, Mizoram University, Mizoram.

BIO-DATA OF THE CANDIDATE

Personal Information:

Name : Vanzarmawii

Father's name : C. Vanlalchhuana

Mother's name : F. Lalawmpuii

Date of Birth : 21.03.1993

Nationality : Indian

Gender : Female

Marital Status : Single

Present Address : House No. A/16, Electric Veng, Aizawl, Mizoram

Subject of Specialisation: High Energy Physics

Educational Qualification:

H.S.L.C : 2009 Distinction M.B.S.E.

H.S.S.L.C : 2011 First Division M.B.S.E.

B.Sc. (Physics) : 2015 First Division N.E.H.U.

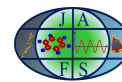
M.Sc. (Physics) : 2017 Distinction A.D.B.U.

Pre-Ph.D Course : 2018 First Division M.Z.U.

Working Experience:

- Completed M.Sc Project work titled, “Reproduction of the Research Paper, A New Super-Soft X-ray Source in the Small Magellanic Cloud: Discovery of the First Be/White Dwarf System in the SMC?” under Mr. Parag Bhattacharya, Department of Physics, Assam Don Bosco University, Guwahati, Assam, 2017.

PUBLICATIONS



Journal of Applied and Fundamental Sciences

GENERATION OF SPECTRAL AND TIMING PROPERTIES OF CYGNUS X-2 USING ASTROSAT'S DATA

Vanzarmawii Chhangte*¹, Ranjeev Misra², Lalthakimi Zadeng¹

¹Department of Physics, Mizoram University, Tanhril-796004, Aizawl, Mizoram, India

²Inter-University Centre for Astronomy and Astrophysics, Geneshkhind, Pune-411007, India

*For correspondence. (zarichhangte0739@gmail.com)

Abstract: We present here AstroSat LAXPC and SXT observation of an X-ray Binary source focusing on neutron stars. X-ray binaries are a class of binary stars, so-called because they emit X-ray. These X-rays are produced by matter falling from one component called donor to another component, accretor. The donors are usually normal stars and accretor are collapsed stars which are very compact e.g. neutron stars, white dwarf or black hole. We have taken into study, Cygnus X-2, which is a 9.84 day period neutron star binary belonging to long-period low-mass X-ray binary type. It is one of the brightest and longest known X-ray source. Three observations are studied for which lightcurves are generated with time bin of 100s each for LAXPC and 23s each for SXT. Hardness ratios are plotted from the generated lightcurve. Spectra and power spectra are also generated within the energy range 4.0-80.0 keV for LAXPC and 0.3-8.0keV for SXT. Further analysis of these spectral and timing properties will be done. For timing analysis, Fourier transform is used and spectra will be fitted using χ^2 fitting.

Keywords: accretion; accretion discs; stars: neutron; stars: individual: Cygnus X-2; X-rays: binaries

1. Introduction:

Binary stars are two stars orbiting around a common center of mass. The brighter is classified as the primary star and the dimmer is classified as secondary star. Matter is accreted from the companion by the compact object through Roche Lobe overflow or stellar wind accretion. The accreted matter from the companion flows onto the compact star through the influence of its gravitational potential. The inflowing matter has an accretion rate associated with it, so it spirals into the compact star forming an accretion disk. Because of the violent collisions between the particles in the inflowing matter the gas is heated to very high temperatures of about 10^7 K to 10^8 K. It is through this process that the gravitational potential energy of the infalling matter gets converted to the kinetic energy and then into radiation in the form of X-rays.

X-ray Binaries(XRB) are of two types depending on the mass of the mass losing star (companion star): Low-mass XRB (LMXB) and High-mass XRB (HMXB). In LMXB the donor star have a mass of about $1M_{\odot}$. LMXB fill their Roche lobe and transfer of mass takes place by accretion of matter through inner Lagrangian point. The neutron star here has weak magnetic field of about 10^7 to 10^9 Gauss, therefore the accreted matter does not fall onto the magnetic poles. They have a very pronounced accretion disk and a vast majority of the produced X-rays are from the inner part of the disk and the surface of the neutron star. X-rays are also found to be produced from the accretion disk corona which is the extended region above and below the disk. The wind material driven off of the disk produces extended corona. X-rays are scattered by hot plasma in the disk from the corona.

In HMXB, the donor star have mass $\leq 10M_{\odot}$. Most of its mass is lost due to powerful stellar wind of the companion star. Mass transfer in HMXB systems takes place by powerful accretion of some part of the matter from the stellar wind of the companion star by the compact object. They do not have distinct accretion disk and the accretor in HMXBs may be a neutron star or a black hole. Here the neutron stars have high magnetic field of about 10^{12} Gauss.

The source, Cygnus X-2 is a LMXB, consisting of a neutron star with an optically measured mass of $M_x > 1.78 \pm 0.23M_{\odot}$ [3] orbiting around V1341 Cyg with an orbital period of ~ 9.8 days [1, 2]. Cyg X-2 is a bright



AstroSat detection of a quasi-periodic oscillation at ~ 42 Hz in Cygnus X-2

Vanzarmawii Chhangte,^{1*} Jayashree Roy¹, Ranjeev Misra² and Lalthakimi Zadeng¹

¹Physics Department, Mizoram University, Tanhril, Aizawl, Mizoram 796004, India

²Inter-University Center for Astronomy and Astrophysics, Post Bag 4, Pune, Maharashtra 411007, India

Accepted 2022 February 9. Received 2022 January 26; in original form 2021 December 10

ABSTRACT

We report the results of *AstroSat* observations of Cygnus X-2 during 2016 February. The source's power density spectrum generated using Large Area X-ray Proportional Counter (LAXPC) data revealed the presence of a prominent quasi-periodic oscillation (QPO) at ~ 42 Hz with broad-band continuum noise at lower frequencies at ~ 10 Hz. The large effective area of LAXPC at $\gtrsim 30$ keV allowed for an unprecedented study of the energy dependence of the QPO and the broad noise continuum. The fractional rms increases with energy, and its shape is similar for both the QPO and the continuum noise, suggesting a common radiative origin. However, while the QPO exhibits hard time-lags, with the high-energy photons lagging the low ones by a few milliseconds, the continuum noise shows the opposite behaviour. The photon spectrum from *Soft X-ray Imaging Telescope* and LAXPC in 0.7–30 keV band comprises the soft component from a disc and a hard Comptonized component from a hot corona. While the energy dependence of the rms shows that the QPO and the continuum noise variability are dominated by the Comptonized component, the change in sign of the time-lag suggests that the dynamic origin of the QPO may be in the disc while the noise continuum may originate from the corona.

Key words: accretion, accretion discs – stars: individual: Cygnus X-2 – stars: neutron – X-rays: binaries.

1 INTRODUCTION

X-ray binaries are a class of binary stars, so-called because they emit X-rays. The binary star comprises of a companion star and an accretor. These X-rays are produced by matter falling from the donor star to the accretor. The donors are usually normal stars, and accretors are collapsed stars that are compact, e.g. neutron stars (NSs), white dwarf, or black holes (BHs). The X-ray binaries are classified into two classes according to the masses of the companion star: high-mass X-ray binary and low-mass X-ray binary (LMXB).

The X-ray binary system comprising a NS as a compact object and a low-mass star as its companion is classified as a NS LMXB. These can be subdivided into Z-type and Atoll-type sources based on X-ray spectral and fast timing behaviour (Hasinger & van der Klis 1989). The Z sources trace out a Z-shape in the X-ray colour–colour diagram (CCD). The branches of the Z-type sources are horizontal branch (HB), normal branch (NB), and flaring branch (FB), from top to bottom. The Z sources are classified into two groups (Hasinger & van der Klis 1989; Kuulkers et al. 1997): (i) the Cyg-like sources – Cyg X-2, GX 5-1, and GX 340+0 – where the HB, NB, and FB are seen but with weak flaring and (ii) the Sco-like sources – Sco X-1, GX 349+2, and GX 17 + 2 – where flaring is strong and frequent but with a short or weak HB.

A characteristic feature of these sources is their rapid nearly sinusoidal variation which is revealed by peaks in their power spectra known as quasi-periodic oscillations (QPOs). In the HB, the frequencies of the QPO vary between ~ 15 and ~ 55 Hz (Alpar & Shaham 1985; Lamb 1989; Ghosh & Lamb 1992), while in the

NB, the frequencies range between 5 and 7 Hz, and in the FB, the frequencies are observed to increase from ~ 6 up to ~ 20 Hz along the branch (Hasinger 1990). The sources also exhibit high-frequency kHz QPOs, which sometimes occur in pairs (Wijnands et al. 1998; Kuznetsov 2002). Despite several endeavours to characterize the phenomena, there is at present no consensus on the origin of these different kinds of QPOs.

Byram, Chubb & Friedman (1966) first discovered Cygnus X-2 (henceforth Cyg X-2) using the sounding rocket experiment. It was first observed by *EXOSAT* for a continuous duration of 14 h starting on 1984 July 23, using gas scintillation proportional counter (Peacock et al. 1981) and one-half of medium energy detectors (Turner, Smith & Zimmermann 1981). The X-ray binary source – Cyg X-2, is a bright, persistent LMXB. Cyg X-2 is classified as a Z-type source because of its behaviour and pattern when studied on an X-ray CCD and hardness–intensity diagram (HID; Hasinger & van der Klis 1989; Hasinger 1990; Van der Klis 2000). After the observation of thermonuclear X-ray bursts in Cyg X-2, its compact companion was identified as a NS with a low magnetic field (Kahn & Grindlay 1984; Smale 1998), its mass is measured as $M_x > 1.78 \pm 0.23 M_\odot$ (Orosz & Kuulkers 1999). The binary system has a late-type companion, V1341 Cyg with an orbital period of ~ 9.8 d (Cowley, Crampton & Hutchings 1979; Casares, Charles & Kuulkers 1998) and a mass ranging between 0.4 and 0.7 M_\odot whose spectral type seem to vary from A5 to F2 (Cowley et al. 1979).

QPOs as well as broad continuum noise features have been extensively observed in Cyg X-2, by timing studies carried out using the proportional counter array onboard the *RXTE* satellite (Wijnands et al. 1998). Simultaneous detection of twin peaks at 500 and 860 Hz and the highest single kHz QPO at 1007 Hz were reported by

* E-mail: zarichhange0739@gmail.com

PARTICULARS OF THE CANDIDATE

NAME OF CANDIDATE : VANZARMAWII

DEGREE : DOCTOR OF PHILOSOPHY

DEPARTMENT : PHYSICS

TITLE OF THESIS : SPECTRAL TIMING STUDIES
OF X-RAY BINARIES OBSERVED
WITH ASTROSAT

DATE OF ADMISSION : 16.08.2018

APPROVAL OF RESEARCH PROPOSAL :

1. DRC : 28.03.2019
2. BOS : 15.04.2019
3. SCHOOL BOARD : 08.05.2019

MZU REGISTRATION NO. : 1807323

Ph. D. REGISTRATION NO. : MZU/Ph.D./1263 of 16.08.2018
AND DATE

EXTENSION : NIL

(Prof. Zaithanzauva Pachuau)

Head

Department of Physics

ABSTRACT

**SPECTRAL TIMING STUDIES OF X-RAY BINARIES
OBSERVED WITH ASTROSAT**

**AN ABSTRACT SUBMITTED IN PARTIAL FULFILMENT OF
THE REQUIREMENTS FOR THE DEGREE OF DOCTOR OF
PHILOSOPHY**

VANZARMAWII

MZU REGISTRATION NUMBER : 1807323

Ph.D. REGISTRATION NUMBER : MZU/Ph.D./1263 of 16.08.2018



**DEPARTMENT OF PHYSICS
SCHOOL OF PHYSICAL SCIENCES
APRIL, 2024**

**SPECTRAL TIMING STUDIES OF X-RAY BINARIES OBSERVED WITH
ASTROSAT**

By

Vanzarmawii

Department of Physics

Name of Supervisor: Dr. Lalthakimi Zadeng

Name of Jt. Supervisor: Prof. Ranjeev Misra

Submitted

**In partial fulfillment of the requirement of the Degree of Doctor of
Philosophy In Physics of Mizoram University, Aizawl.**

ABSTRACT

This thesis focuses on the spectral and timing studies of X-ray binary source. This abstract provides an overview of a neutron star low mass X-ray binary source, Cygnus X-2. As a neutron star low-mass X-ray binary source, this system involves a neutron star and a lower-mass companion star engaged in a dynamic dance of mass transfer. The neutron star at the heart of Cygnus X-2, a remnant of a massive star's supernova explosion, exhibits extreme density, resulting in the emission of intense X-rays. Interacting with a lower-mass companion star, the system manifests as an X-ray binary due to the transfer of mass from the companion to the neutron star. This mass transfer leads to the formation of an accretion disk around the neutron star. In Cygnus X-2 the two stars are in a close orbit, and their gravitational interaction plays a crucial role in the exchange of mass between them. The lower-mass companion star in Cygnus X-2 fills its Roche lobe, a region around the star where gravitational forces favor mass transfer toward the neutron star. This overflow of material from the companion star is a consequence of the gravitational influence of the neutron star, causing the material to flow towards the more massive neutron star. As the material from the companion star moves towards the neutron star, it forms an accretion disk around the neutron star. The accretion disk is a rotating disk of gas and dust spiraling inward due to gravitational forces. This disk is a crucial component in the mass transfer process and serves as the source of X-ray emissions observed from the system. The mass transfer in Cygnus X-2 leads to the accretion of material onto the neutron star. As the material falls onto the neutron star's surface, it releases a significant amount of gravitational potential energy. This energy is emitted in the form of X-rays, making Cygnus X-2 a prominent X-ray binary source.

This abstract focuses on Cygnus X-2's distinct traits and behaviours, notably classifying it as a Z-type neutron star low-mass X-ray binary source. The abstract investigates the distinguishing characteristics of Z-type behaviour, offering light on the complicated accretion processes and rich phenomenology found in this mysterious astronomical system. The appearance of various branches in the X-ray hardness-intensity diagram, indicating tran-

sitions between different accretion states, characterises this behaviour. The abstract digs into the significance of these branches, revealing the mechanisms that govern the accretion processes in this binary system.

Using AstroSat's observation, timing and spectral studies of X-ray binary have been carried out in this thesis. The instrumentation process involves data collected by LAXPC and SXT onboard AstroSat. Using pipelines of both these instruments, data reduction was done. The data analysis technique consists of the timing analysis done using Fourier transform and a spectral analysis done using XSPEC.

The Fourier Transform is a powerful mathematical technique that bridges the time and frequency domains in a variety of applications. It decomposes a time-domain function or signal into its constituent frequencies. The Fourier Transform, which is based on the idea that any complex waveform can be represented as a sum of sinusoidal functions, allows for the study of signals in the frequency domain, revealing hidden patterns and characteristics. The abstract dives into the Fourier Transform's mathematical roots, explaining the continuous and discrete formulations. The integral and summation transforms translate time-dependent signals into frequency representations, providing insights into the spectral content and frequency distribution of a particular signal. The assessment of a signal's frequency content to reveal vital information about underlying processes is a cornerstone in signal processing and scientific investigation.

Here we explain core spectral analysis procedures such as the Fourier Transform, power spectral density, and related techniques. It delves into both time and frequency domain representations, demonstrating how spectrum analysis can dissect signals and reveal hidden patterns in large datasets. The purpose of spectral analysis is to use various physical models to explore the shape of the energy continuum. The Xspec (X-ray Spectral Fitting programme) component of HEASoft allows spectra to be fitted using a variety of models supplied in the programme. During the fitting procedure, some local models can be used. Spectra collected by a detector do not reveal the true spectrum of a source due to the effect of the detector's response and effective area. To determine the true source spectrum, the

recorded photon distribution is merged with the detector response. The XSPEC is used to match the source spectra using the χ^2 technique with suitable background subtraction, response, and effective area files.

The time-lags identified in this work for the $\sim 42\text{Hz}$ QPO are in the order of $\sim 5\text{ms}$, making compton scattering effects implausible unless the size of the corona for this observation is ~ 100 times higher than when a kHz QPO is detected. Significantly longer time lags than those caused by light travel time effects can be explained in a framework in which both the seed photon source and the Comptonizing medium vary coherently with a time lag between them. For example, a model in which the corona heating rate and seed photon temperature vary coherently with a time delay between them can predict and fit the observed energy dependent r.m.s and time-lag for broad band noise and QPO of black hole systems. One clear and generic property of such models is that hard lags occur when the coronal variation is delayed in comparison to the soft photon source, and soft lags occur when the coronal variation is delayed in comparison to the soft photon source.

In this study, we discovered that whereas broad band noise at 10Hz has soft delays, 42Hz QPO exhibits strong lags. The most basic explanation is to use causation and argue that broad band noise is formed in the corona and propagates to the soft photon source, whereas QPO is generated in the soft photon source and propagates to the corona.

If the soft photon source is assumed to be an accretion disc surrounding the Comptonizing medium, it is interesting to note that while broad band noise is produced in the tenuous corona, the disc produces narrow coherent QPO, making it tempting to associate the QPO frequency with the inner disc radius. The inner radius of the disc can be estimated as $R_{in} \sim 45\text{kms}$ using the best fit value of the disc normalisation $n \sim 70$ and a distance, $D \sim 13.5\text{kpc}$, inclination angle, $i \sim 60^\circ$, and colour factor, $f \sim 1.7$. The Keplerian frequency at that radius for a neutron star mass of $1.4M_\odot$ equals $\sim 240\text{Hz}$. The radius at which the Keplerian frequency equals the $\sim 42\text{Hz}$ QPO frequency is $\sim 140\text{kms}$. Given the uncertainty in the spectral fitting, the spectral model utilised, and the colour factor, it is possible that the QPO is connected with the inner disc radius's Keplerian frequency.

It could also be related with one of the other lower frequencies found in that radius. Nonetheless, the findings of this study suggest that the QPO originates in the soft photon source and may be related with some characteristic time-scale of the inner disc radius. In this work, we see that the source was in various part of the branch for different set of observations. Most of the branch follows that the soft component increases as we move from left to right along the branch. We see that the temperature is lowest at the soft apex 1.2, this suggests that the mass accretion rate is low. Also at this point R_{in} is maximum at 10.5km for a set of observation and maximum at 17.7km for another set of observation, which is found to be consistent with the whole neutron star surface being emitting. So in our spectral deconvolution, they can be ascribed to a variation of the soft blackbody component, and this becomes harder as they move along from left to right along the branches. From here we interpret the soft blackbody component in the spectra of the Z sources as emission from inner accretion disk. However, the inner disk is found to be decreasing in some case. This can be explained by an occultation of the Comptonizing region probably caused by matter in an inner flared disk, or by an evolution from a spherical to non-spherical geometry of the Comptonising cloud.